Geochimica et Cosmochimica Acta 397 (2025) 188–204

Contents lists available at ScienceDirect

Geochimica et Cosmochimica Acta

journal homepage: www.elsevier.com/locate/gca

Multiple episodes of serpentinite alteration revealed by progressive leaching experiments

Aled D. Evans [a,*], Matthew J. Cooper [a], Dave Craw [b], Damon A.H. Teagle [a]

[a] School of Ocean and Earth Science, National Oceanography Centre Southampton, University of Southampton, Southampton, UK
[b] Department of Geology, University of Otago, Dunedin, New Zealand

ARTICLE INFO

Associate editor: Frieder Klein and Hailiang Dong

Keywords:
Serpentinization
Leaching experiments
Alteration events
Mantle rocks

ABSTRACT

Serpentinized mantle rocks typically experience multiple alteration events, but to date, identifying distinct serpentinization episodes remains difficult because whole rock geochemical and isotopic analyses reflect the cumulative sum of fluid-rock interactions. Here we unravel the alteration history of serpentinized mantle rocks by undertaking multi-stage progressive leaching experiments to isolate distinct geochemical and $^{87}Sr/^{86}Sr$ signatures hosted within serpentinized peridotites from the Troodos Mantle Sequence and Limassol Forest Complex, Cyprus that have different geological histories. Whole rock powders underwent an initial 10 % acetic acid solution leaching step before a subsequent 3 M HCl treatment. The remaining residue was then completely dissolved and analysed following a standard HF and HNO_3 digestion. For comparison an untreated sample of whole rock powder was also completely digested and analysed. In the Troodos Mantle Sequence, an initial serpentinization event with relatively primitive $^{87}Sr/^{86}Sr$ ratios (0.705 to 0.706) is recorded by the rock residues and is consistent with alteration by fluids sourced from the dehydrating downgoing Cyprus slab. A more radiogenic $^{87}Sr/^{86}Sr$ (0.7086–88) signal, consistent with Cyprus Messinian seawater and evaporites, is mobilised by the initial leaching step. These contrasting signatures in the mantle rocks are similar to the Sr-isotopic compositions of Troodos Mantle Sequence groundwaters. Although previous field observations within the Limassol Forest Complex indicate some serpentinization by Cretaceous seawater, evidence from progressive leaching experiments of pervasive serpentinization on the Cretaceous seafloor is not forthcoming. Our results show that most samples from the Limassol Forest Complex yield a radiogenic $^{87}Sr/^{86}Sr$ signal (0.7087), most consistent with mid-Miocene Messinian seawater and broadly coeval with significant mid-Miocene uplift of the Limassol Forest Complex. These results demonstrate that progressive leaching approaches can reveal distinct alteration episodes with contrasting $^{87}Sr/^{86}Sr$ ratios and geochemical signatures that contribute to the overall integrated bulk rock signal.

1. Introduction

Interactions between mantle rocks and water induce serpentinization reactions that dramatically change anhydrous mantle peridotites into hydrated serpentinites containing up to 13.5 wt% water with affinities for fluid-mobile elements (Kerrick, 2002). As a result, serpentinites act as geological sponges, playing a critical role in global biogeochemical cycles of important components such as H_2O, C, Cl, B, and S (Früh-Green et al., 2004; Schwarzenbach et al., 2012; Alt et al., 2013). Despite its critical role in the Earth system, quantification of the contribution of distinct mantle rock alteration episodes is fraught by uncertainty since knowledge of when, where, and with what fluids serpentinization occurred remains enigmatic.

Serpentinization occurs, to varying magnitudes, in a range of geodynamic settings such as slow spreading mid ocean ridges (e.g., Francis, 1981; Früh-Green et al., 2003; Mével, 2003; Bach et al., 2006), bend faults (Ranero et al., 2003; Ranero and Sallarès, 2004), subduction zones (Fryer et al., 1985; Hyndman and Peacock, 2003), rifted margins (e.g., Boillot et al., 1980; Bayrakci et al., 2016), strike-slip plate boundaries (e.g., Moore and Rymer, 2007) and transform faults (Francis, 1981; MacLeod and Murton, 1993; Cox et al., 2021), and serpentinized massifs within ophiolite sequences (e.g., Barnes and O'Neil, 1969; Wenner and Taylor, 1971, 1973; Magaritz and Taylor, 1974; Evans et al., 2024a, b). However, direct in situ observation and sampling of many of these

* Corresponding author.
E-mail address: A.Evans@soton.ac.uk (A.D. Evans).

https://doi.org/10.1016/j.gca.2025.04.001
Received 28 July 2024; Accepted 2 April 2025
Available online 5 April 2025

settings remains unaccomplished (e.g., Teagle and Ildefonse, 2011). As a result, attention has been focussed on samples that are relatively easily accessible on both land and the oceans, but secondary near-surface processes may overprint and obscure signatures of earlier reactions where the bulk of the serpentinization occurred.

Evidence from cross-cutting relationships combined with trace element determination (Kodolányi and Pettke, 2011; Kahl et al., 2015; Peters et al., 2017; Albers et al., 2020), stable oxygen and hydrogen isotope analyses (e.g., Wenner and Taylor, 1971, 1973, 1974; Peacock, 1987; Burkhard and O'Neil, 1988; Früh-Green et al., 1990; O'Hanley and Offler, 1992; O'Hanley et al., 1992; Agrinier et al., 1996; Kyser et al., 1999; Alt and Shanks, 2006; Nuriel et al., 2009; Ulrich et al., 2020; Scicchitano et al., 2021; Vesin et al., 2023), boron isotopic compositions and $^{87}Sr/^{86}Sr$ ratios (Boschi et al., 2008; McCaig et al., 2010; Harvey et al., 2014; Yamada et al., 2019; Evans et al., 2024b) of near-surface to surface serpentinites are consistent with a progressive series of serpentinization reactions resulting from multiple and distinct water–rock interaction episodes (Hostetler et al., 1966; Coleman and Keith, 1971; Coulton et al., 1995; Bach et al., 2006; Andreani et al., 2007; Schwarzenbach et al., 2012; Cooperdock and Stockli, 2016).

However, to date, establishing the conditions of distinct serpentinization episodes remains challenging since serpentinites are mixtures of the accumulated signatures resulting from their complex geological histories. Early signatures may be obscured by subsequent overprinting alteration episodes (Kyser and Kerrich, 1991). Reactions can both add fluid-mobile components as well as leach them (Bach et al., 2004; Evans

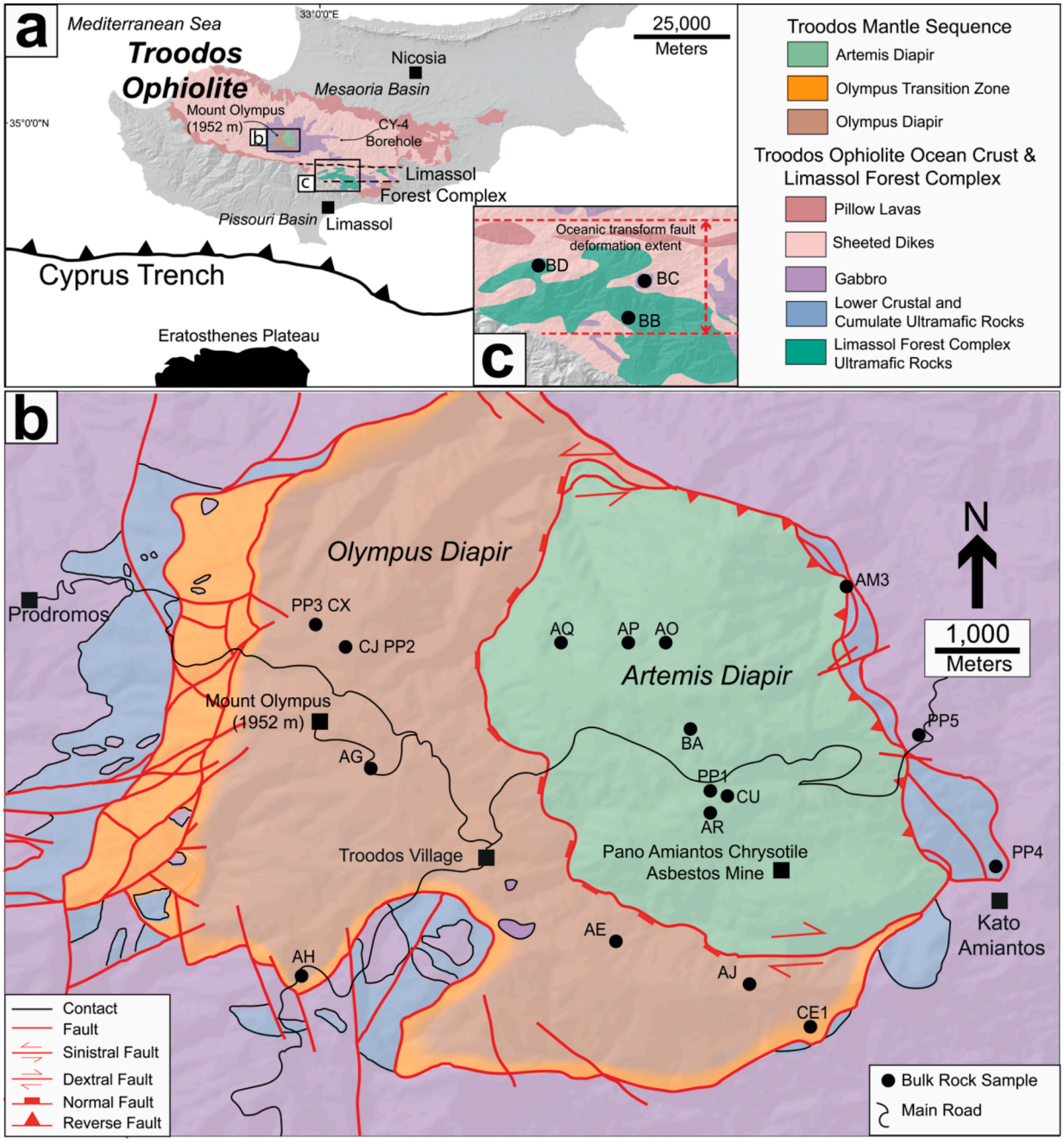

Fig. 1. (a) Geological map of the Troodos ophiolite and Limassol Forest Complex with the bullseye geometry of the Mantle Sequence highlighted and which does not occur in the Limassol Forest Complex. The Cyprus Trench and northernmost extent of the Eratosthenes Plateau are also shown. (b) Geological map of the Troodos Mantle Sequence (updated from Wilson, 1959) with locations of rock samples also shown. (c) Inset map of the Limassol Forest Complex with locations of rock samples and extent of oceanic transform deformation (following Gass et al., 1994) also shown.

et al., 2024a, b). Consequently, traditional whole rock analytical approaches lead to integrated signals that do not necessarily identify the geochemical and isotopic signatures of specific serpentinization episodes.

Unravelling these multistage alteration events requires either in situ analyses (e.g., Vesin et al., 2023; Evans et al., 2024b) or progressive chemical attack and this latter approach is investigated here. Some previous studies (Hostetler et al., 1966; Snow et al., 1993; Bickford et al., 2008; Harvey et al., 2014; Frisby et al., 2016; Nielsen et al., 2024) have applied successive acid solutions of increasing strengths to separate contrasting signatures but these techniques have not been widely or systematically applied. Here we deploy a progressive leaching approach combined with field observations, to establish the contrasting multistage alteration histories of neighbouring geological domains in Cyprus, namely the Olympus and Artemis diapirs of the Troodos Mantle Sequence and the transform fault-related Limassol Forest Complex (Fig. 1). We apply a three-step progressive leaching experiment with acids of increasing strength on bulk whole rock powders (Fig. 2) and show that contrasting geochemical signatures and strontium isotopic compositions are recovered by the respective leaching steps. We demonstrate that whole rock analyses are the cumulative sum of multiple alteration events and distinct signatures of specific events can be isolated and identified by progressive leaching experiments.

2. Geological setting

2.1. Troodos Mantle Sequence

The Troodos mountains expose oceanic crust and upper mantle rocks in a ~90 km-long and ~30 km-wide ophiolite that is one of the world's least deformed, most complete and best-preserved sequences (Gass, 1968). The Troodos ophiolite formed ~90 to 92 Ma at some form of supra-subduction zone spreading ridge in the Neo-Tethyan Ocean (Moores and Vine, 1971; Pearce et al., 1984; Moores et al., 1984; Mukasa and Ludden, 1987). The Troodos Massif crops out as an elliptical bullseye-patterned welt (Fig. 1) with partially serpentinized mantle rocks forming the highest elevations (Mount Olympus, 1952 m asl). The stratigraphically deepest rocks of the Mantle Sequence are surrounded by an eroded anticlinal dome comprising concentric annuli of gabbroic and ultramafic cumulate rocks, sheeted dikes, lavas and conformable submarine sediments at progressively lower elevations. A long-standing subdivision occurs within the Troodos Mantle Sequence (Wilson, 1959; Gass and Masson-Smith, 1963; Moores and Vine, 1971) with the identification of the Olympus and Artemis serpentinite diapirs that have contrasting characteristics resulting from different serpentinization and deformation histories (Evans et al., 2021).

The Olympus Diapir, is an arcuate region of partially serpentinized tectonized harzburgites with minor dunites (Wilson, 1959; Moores and Vine, 1971) and displays a distinctive, competent, blocky, and cohesive outcrop pattern (Fig. 3) that forms rounded, stable hillslopes (Wilson, 1959; Gass, 1977; Evans et al., 2021), interpreted to result from the partial (50 to 70 % replacement of primary phases) serpentinization of mantle peridotites (Evans et al., 2021). Rocks located from the periphery of the Olympus Diapir are more strongly serpentinized (up to ~90 %; Fig. 3). A serpentine-olivine dominated mesh texture is pervasive (Fig. 3) and encloses 1 to 4 mm grains of orthopyroxene partially altered to bastite (Fig. 3a). In more strongly serpentinized samples, the serpentine-olivine-orthopyroxene dominated texture is commonly cross-cut by discrete (~3 mm wide), black (in XPL and hand specimen) serpentine veins (Fig. 3b). These black serpentine veins are irregularly distributed throughout the Olympus Diapir and display a wide range of orientations that are not systematically related to a distinct veinset orientation (Fig. 3b). Samples with higher serpentine contents yield higher trace amounts of carbonate (Fig. 3c) primarily hosted in thin < 20 μm veinlets. The carbonate is predominantly calcium carbonate with rare, thin < 10 μm veinlets of dolomite. Magnesite is rare but occurs in the surface as the infilling matrix of serpentine-magnesite breccias. A complex marginal boundary, termed the Olympus Transition Zone (e.g., Evans et al., 2021), occurs between the Olympus Diapir and the encircling plutonic crustal rocks (Fig. 1b).

In contrast to the Olympus Diapir, the Artemis Diapir is a subcircular, ~5 km-wide region of completely serpentinized peridotite blocks and clasts (>100 m to 0.1 m; approximately 50:50 clasts to matrix) in a friable, low bulk density, serpentinite breccia matrix of highly comminuted serpentine cataclasite and serpentine clay gouge (Wilson, 1959; Gass and Masson-Smith, 1963; Moores and Vine, 1971; Evans et al., 2021). Coherent completely serpentinized blocks and clasts (Fig. 4) are heavily fractured with mutually cross-cutting, orthogonal, concentric, and oblique fibrous asbestiform chrysotile and crack-seal serpentine vein sets occurring within more competent clasts (Fig. 5). The Artemis Diapir competent blocks and clasts are dominated by serpentine (>90 %) with minor secondary andradite (~<5 %) and carbonate (~<5 %) (Fig. 6). Pyroaurite occurs at some sites where hyperalkaline waters seep out of the serpentinite breccia (Evans et al., 2024a). All primary minerals are replaced except for chrome-spinel. In some parts of the Artemis Diapir, serpentinite breccia assemblages

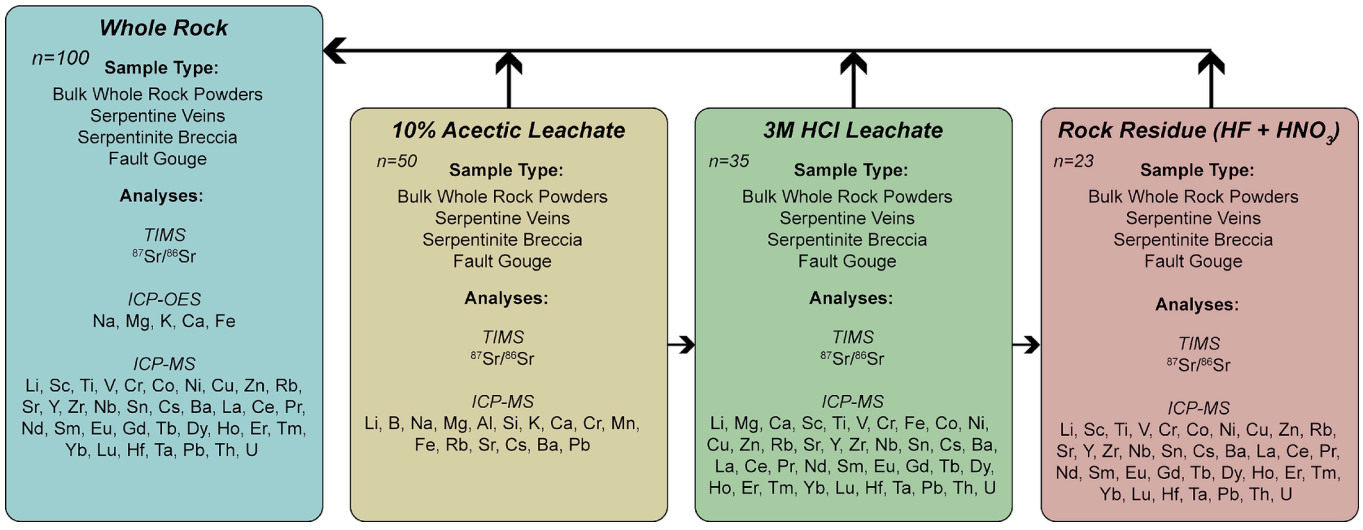

Fig. 2. Summary figure of the multistep progressive leaching experiment methodology, what elements are analysed at each leaching step and by which instrumentation.

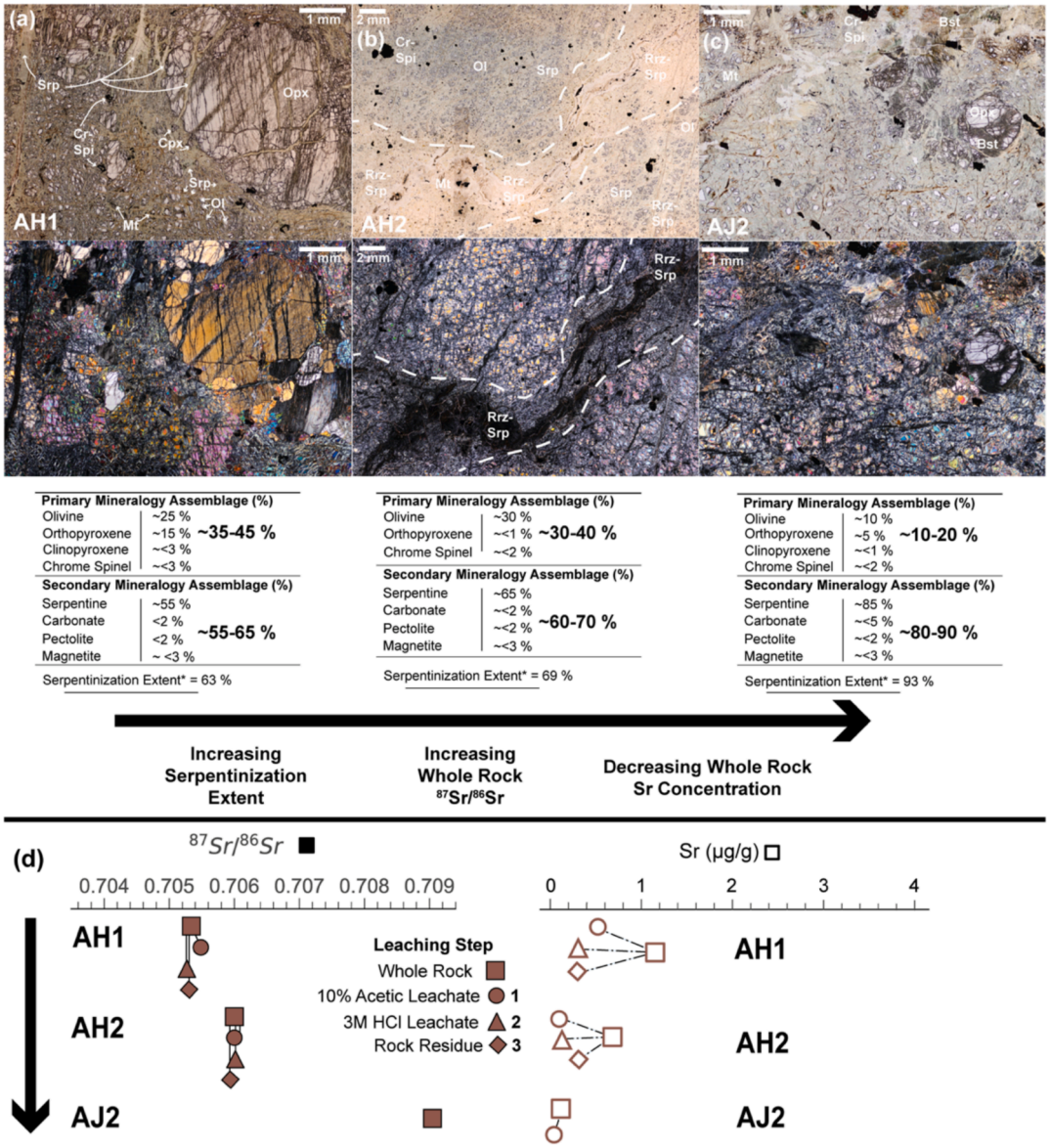

Fig. 3. (a) Photomicrograph in PPL (plane-polarised light) and XPL (cross-polarised light) of Olympus Diapir sample AH1, partly serpentinized harzburgite. (b) Photomicrograph in PPL and XPL of Olympus Diapir sample AH2, partly serpentinized dunite. (c) Photomicrograph in PPL and XPL of Olympus Diapir sample AJ2, strongly serpentinized harzburgite. PPL and XPL photomicrographs show a general increase in recrystallised serpentine manifested as irregular black serpentine veins. Serpentinization extent is calculated using the equation of Miller and Christensen (1997) and respective bulk density data (Evans et al., 2021). These photomicrographs show increasing extents of serpentinization (a-c) that correspond to (d) increases in whole-rock $^{87}Sr/^{86}Sr$ and decreasing Sr (ng/g) concentration. We note that brucite was not observed in thin section or through SEM-EDS. Abbreviations follow as: Srp = serpentine, Rrz = recrystallized, Bst = bastite, Opx = orthopyroxene, Mt = magnetite, Cr-Spi = chrome spinel, ol = olivine. (d) Plots of $^{87}Sr/^{86}Sr$ (filled squares) and Sr (µg/g; open squares) for the bulk rock digestion (square) and each progressive leaching step (circle – 10 % Acetic; triangle – 3 M HCl; diamond – residue).

surround and anastomose around completely serpentinized competent blocks and clasts (Evans et al., 2021). In some zones, around the periphery of the Artemis Diapir, the proportion of incompetent breccias-gouge to competent blocks-clasts is dominated by the serpentinite breccia-gouge assemblage, resulting in an easily erodible low-density serpentinite breccia endmember (e.g., Wilson, 1959; Evans et al., 2021). The formation of this end member is attributed to progressive coupled deformation-alteration-recrystallization serpentinization producing weak, unstable, incohesive outcrops and hillslopes and deeply incised-valleys that are characteristic of the Artemis Diapir (Evans et al., 2021).

The focused uplift and exposure of the Troodos massif is relatively recent (since ~5.5 Ma; (Robertson, 1977; McCallum, 1989; Poole and Robertson, 1991, 1998; Stow et al., 1995; Rouchy et al., 2001) and concomitant with serpentinization of the Troodos Mantle Sequence (Gass and Masson-Smith, 1963; Moores and Vine, 1971; Robertson, 1977, 1998b; Evans et al., 2021, 2024a). Stable oxygen, hydrogen, and boron isotope analyses and in situ boron element mapping (Magaritz and Taylor, 1974; Heaton, 1976; Sheppard, 1980; Nuriel et al., 2009; Evans et al., 2021, 2024b) are consistent with serpentinization by a slab-derived fluid with further alteration since the Pleistocene resulting from the infiltration of meteoric water once the Troodos massif was exposed at high altitudes (Robertson, 1977; McCallum, 1989; Poole and Robertson, 1991; Stow et al., 1995).

The Cyprus slab is proposed to be the leading edge of the Sinai plate involved in a north-dipping subduction zone consuming old (at least Mesozoic; Müller et al., 2008; Granot, 2016) oceanic crust south of the island of Cyprus (Fig. 1), with initiation of subduction occurring in the

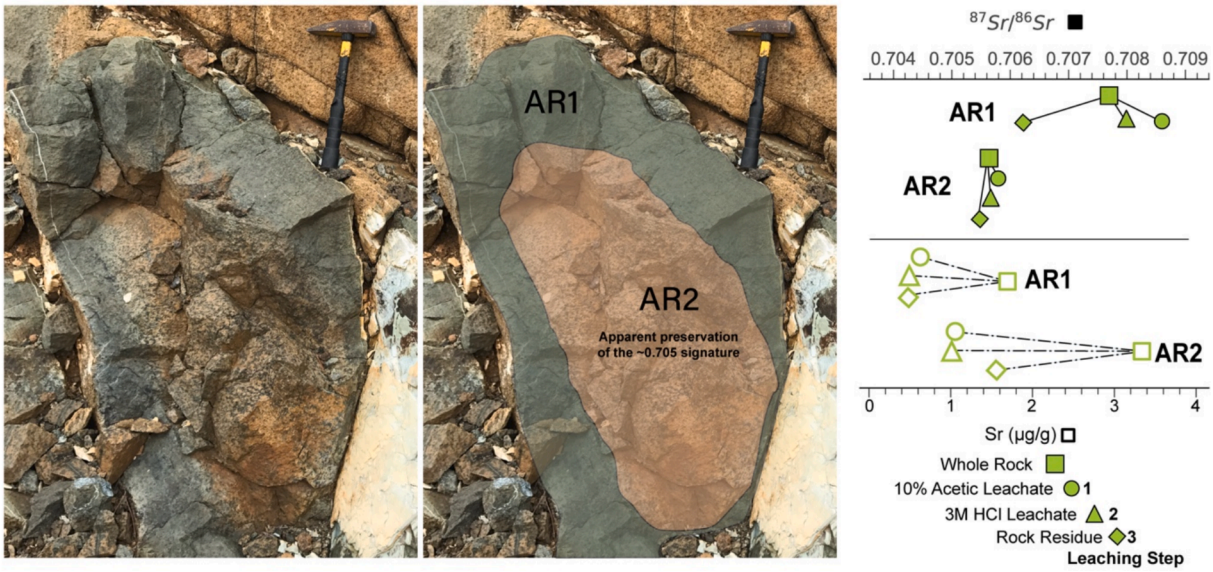

Fig. 4. Unannotated and annotated field outcrop of site AR of the Artemis Diapir with plots of $^{87}Sr/^{86}Sr$ and Sr (µg/g) shown at each progressive leaching step and whole rocks.

early Miocene (~20 Ma; Robertson, 1998b; Feld et al., 2017). Subduction of the Cyprus slab stalled as a result of the collision with the Eratosthenes plateau and the Cyprus trench some ~<5 million years ago (Kempler and Ben-Avraham, 1987; Robertson, 1998b, a, c; Ergün et al., 2005). The depth of the downgoing slab beneath the Mount Olympus region is estimated between ~10 and ~36 km (Mackenzie et al., 2006; Feld et al., 2017; Hayes et al., 2018; Kounoudis et al., 2020) with a slab dip ranging between 13 and 33° (Mackenzie et al., 2006; Feld et al., 2017). These depths are similar to the proposed explanation of the large negative Bouguer anomaly that is centred on the Artemis Diapir and best modelled as a cylindrical vertical body of low density, ~2,700 kg/m^3 strongly serpentinized mantle peridotite extending to ~11 km depth (Gass and Masson-Smith, 1963; Shelton, 1993; Evans et al., 2021).

Groundwaters issuing from the Troodos Mantle Sequence have distinct signatures. Rare, meteoric-derived hyperalkaline (up to pH 13) groundwaters have high salinities and yield $^{87}Sr/^{86}Sr$ ratios of 0.705. The high salinity and $^{87}Sr/^{86}Sr$ of these fluids are reminiscent of end-member hyperalkaline fluids being emitted in serpentinite seamounts in the Mariana forearc, and, by analogy, it has been proposed that these signatures are consistent with dehydration reactions within the downgoing Cyprus slab (Evans et al., 2024a). In contrast, surface waters draining the Troodos Mantle Sequence are relatively fresh and have $^{87}Sr/^{86}Sr$ ratios similar to Cyprus Messinian evaporites (~0.7087; Schildgen et al., 2014) and likely reflect the dissolution of easily mobile salts and carbonates (Evans et al., 2024a).

2.2. Limassol Forest Complex

The Limassol Forest Complex (Fig. 1c) is an area of ~400 km^2 located to the southeast of the Troodos mountains and experienced a different magmatic and deformation history to the Troodos Massif (e.g., Moores and Vine, 1971; Murton, 1986; MacLeod et al., 1990; MacLeod and Murton, 1993). The Limassol Forest Complex is a broad region of deformation much of which is interpreted to have occurred on the Cretaceous seafloor associated with the Arakapas (paleo) Transform Fault. This feature is a prominent W-E trending oceanic dextral strike slip fault zone that is at least 5 km wide and traceable along strike for ~60 km (e.g., Moores and Vine, 1971; Murton, 1986; MacLeod et al., 1990; MacLeod and Murton, 1993; Gass et al., 1994; Fagereng and MacLeod, 2019). Within the Limassol Forest Complex, W-E trending, sub-vertical (Fig. 7a) dextral serpentinite shear zones are common (Murton, 1986; MacLeod, 1988; MacLeod and Murton, 1993). In contrast to the Troodos Massif, there is geological evidence that some of the mantle rocks of the Limassol Forest Complex were serpentinized at or near the Cretaceous seafloor with ultramafic and mafic dikes intruding previously serpentinized mantle peridotites (e.g., Murton, 1986; MacLeod, 1988; MacLeod et al., 1990; MacLeod and Murton, 1993; Martin et al., 2023). These Cretaceous seafloor structures are cut by Miocene uplift-related deformation (Murton, 1986; MacLeod, 1988; MacLeod and Murton, 1993; Martin et al., 2023) with focussed uplift of the Limassol Forest Complex occurred in the mid-Miocene (~14 Ma) as a result of compression from the initiation of modern subduction (~20 Ma; Robertson, 1977, 1998a, b; Eaton and Robertson, 1993). Continued emergence and uplift of the Limassol Forest Complex continued through the Pliocene and Pleistocene with igneous-derived clasts deposited in sedimentary sequences surrounding the complex (Robertson, 1977; Poole and Robertson, 1998; Davies, 2001). In contrast to the Troodos massif, the Limassol Forest Complex does not have a negative bouguer gravity anomaly.

3. Methods

100 bulk rock, vein, breccia, and fault gouge samples were collected from the Troodos Massif, Cyprus. Samples were prepared at the National Oceanography Centre Southampton (NOCS), University of Southampton. Samples were sawn to remove surficial weathering horizons and cut surfaces ground to remove contamination from the saw blade. Samples were then washed and ultra-sonicated (exposed to high frequency sound waves to remove surface contaminants) in Milli-Q 18.2 MΩ cm^{-1} water and left to dry overnight in an oven at 65 °C. Chrysotile veins were not ultra-sonicated. After drying, samples were crushed using a manual iron fly-press, with samples wrapped in paper between plastic chopping boards to reduce trace metal contamination. Samples were then powdered using a chrome-steel jar mill and puck in a Rocklabs mill.

Progressive leaching experiments (Table S1, S2, S3, S4, S5) were undertaken on weighed (0.500 to 3.000 g) aliquots of serpentinized peridotite rock powder. The initial leaching step was the addition of a 10 % Romil UpA acetic acid solution to rock powders, which was left for 48 h at room-temperature and shaken periodically (Fig. 2). Samples were then centrifuged and the leachate removed, dried down, and appropriately diluted (total dilution factor of 300) in 3 % thermally distilled HNO_3. A 3 M HCl solution was added to the leached powders

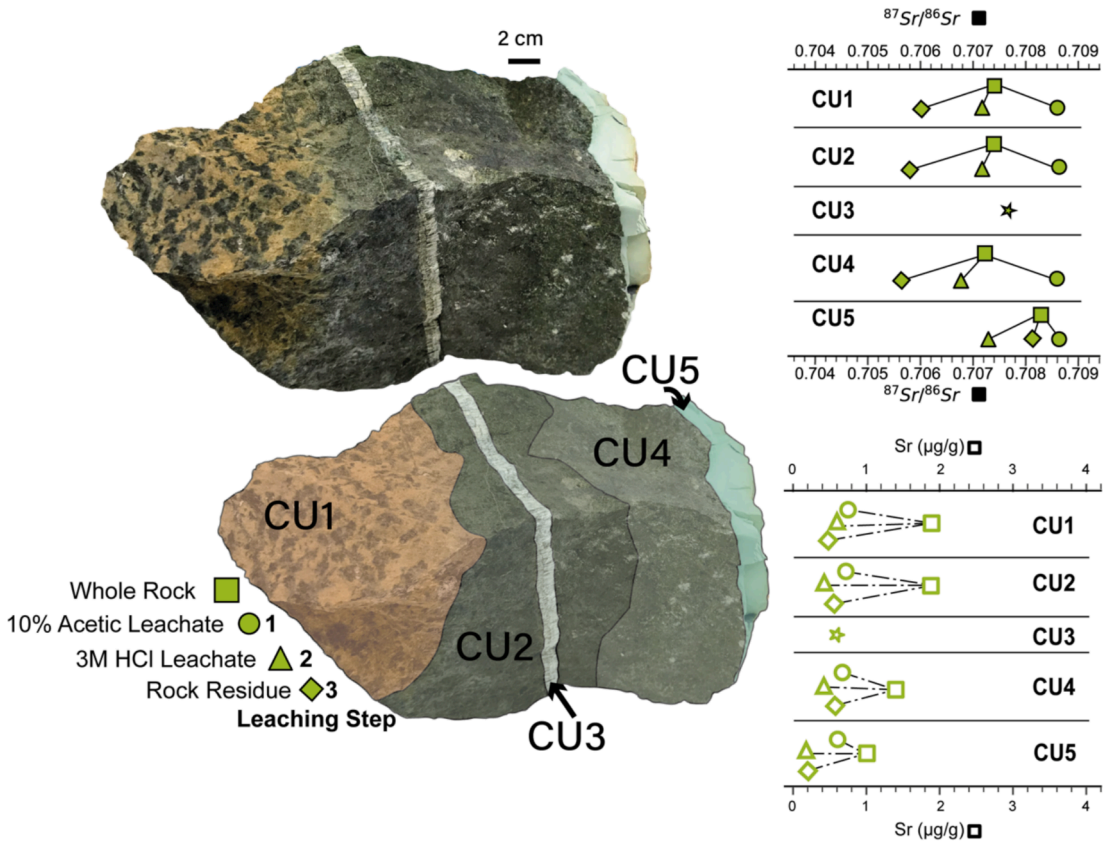

Fig. 5. Unannotated and annotated images of sample CU of the Artemis Diapir with plots of $^{87}Sr/^{86}Sr$ and Sr (µg/g) of each progressive leaching step and whole rocks. CU1 shows a completely serpentinized core with a variably oxidized mesh-texture and less oxidised regions reflecting bastites. CU2 shows a grey completely serpentinized alteration halo. CU3 shows a fibrous chrysotile vein. CU4 shows a completely serpentinized region with extensive serpentine recrystallization. CU5 shows a polygonal serpentine vein.

and left for 48 h at room-temperature (Fig. 2). Samples were then centrifuged, and the 3 M HCl leachate removed, dried down, and appropriately diluted (total dilution factor of 3000) in 3 % thermally distilled HNO_3. 200 mg of the remaining residues were dissolved using a standard HF-HNO_3 digestion in two separate (100 mg each) pots (Fig. 2). In addition, the untreated original bulk rock powders were completely digested following the same method as bulk residues (Fig. 2). The solutions produced from each step were dried down and then dissolved in 3 % HNO_3 containing In, Re and Be to act as internal standards ready for analysis. The acids used were prepared from concentrated acids purified by sub boiling distillation in Savillex CST-1000 stills, except for the HF which was Romil SpA grade.

The 10 % acetic acid solution was expected to mobilise primarily calcium carbonates but also brucite, magnesite, and potentially other hydroxides such as iowaite (Hostetler et al., 1966; Klein et al., 2020; Nielsen et al., 2024). Subsequent addition of 3 M HCl acid was expected to gently attack and leach serpentine with the final residue digesting the remaining serpentine. The 10 % acetic acid leachate, 3 M HCl leachate, and residue concentrations are reported on a per gram basis. The mass of each leaching step was calculated by multiplying the analysed concentration and leaching acid volume, and then normalized by the mass of the original rock powder to yield respective leaching step concentrations. Summing the reported concentration of each step results in a total concentration value directly comparable to the overall bulk rock. The mass balance errors (predicted whole rock/measured whole rock) of each sample, element and $^{87}Sr/^{86}Sr$ ratios are reported in the supplementary materials (Table S6, S7, S8). Following progressive leaching steps, the mean mass balance error of Sr concentrations from all geological domains is 0.9 ± 9 % (1σ; n = 19; Table S6). The corresponding mean mass balance error of $^{87}Sr/^{86}Sr$ ratios is 0.01 ± 0.01 % (1σ; n = 19; Table S6). This shows good recovery of Sr and respective isotopic signatures corresponding to individual leaching steps and that each leaching step add up to the total Sr originally available in the untreated whole rock sample. These mass balance errors also demonstrate that isolated isotopic signatures during our progressive leaching experiments are not artefacts of contrasting leaching systematics. Trace fluid mobile elements such as Li, Rb, Cs, and Ba yield variable mean mass balance errors of < 10 ± <20 % (1σ; Table S8) with individual mass balance errors of some samples of Rb and Ba up to ± 40 % (Table S8). These mass balance errors are likely the result of aggregating the analytical uncertainty of multiple analyses and inherent heterogeneities within the homogenised rock powders. Despite these mass balance errors, our results show that mass balance is generally maintained during progressive leaching.

Rock and vein (including leachates) trace element concentrations were measured by inductively coupled plasma-source mass spectrometry (ICP-MS; Thermo X-Series II) at NOCS and calibrated using international rock standards with In, Re, Be used as internal standards. Precision and accuracy were determined with international rock standards UB-N and JA-2 (Table S5) (Jochum et al., 2005) and internal rock standards BAS-206 and BRR-1. Rock and vein major element concentrations were also measured by inductively coupled plasma optical emission spectrometry (ICP-OES; Thermo Scientific iCap 6000 series) at NOCS and calibrated using gravimetrically prepared synthetic standards. For the majority of elements precision and accuracy were better than ± 5 %RSD and ± 10 % respectively (Table S5).

To determine $^{87}Sr/^{86}Sr$ ratios, an aliquot of dissolved rock equivalent to 500 µg of Sr (100 to 450 mg of rock powder; due to the low Sr concentrations of the rock samples) was dried down and redissolved in 2.2 M HCl onto an initial 7 mL cation exchange column filled with BioRad

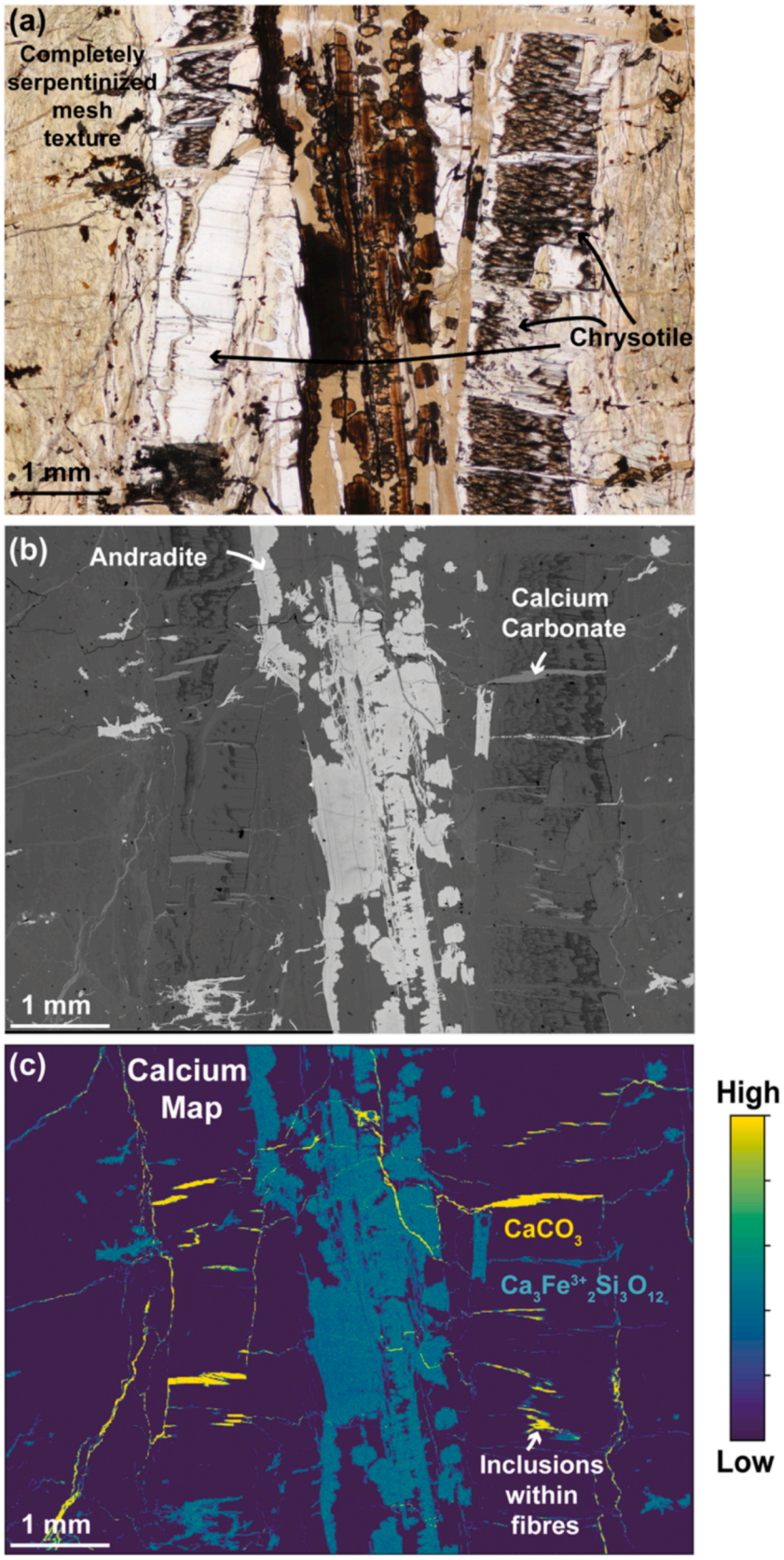

Fig. 6. Plane-polarised Light (PPL) photomicrograph of an Artemis Diapir sample composed of completely serpentinized mesh texture and a multi-stage chrysotile-serpentine vein with secondary andradite. (b) SEM image of the same photomicrograph area with bright areas reflecting andradite and calcium carbonate. (c) SEM-EDS Calcium concentration map with the relative differences mapped using a linear colour scale. Note the acicular inclusions of calcium carbonate occurring within the chrysotile fibres.

AG50W-X12 cation exchange resin to elute high concentration major elements (e.g., Mg, Fe). After passing through the column, samples were collected and dried down and redissolved in 3 M HNO_3 (samples with Ba/Sr > 1 were redissolved in 8 M HNO_3) and Sr was separated using a second-stage Triskem Sr-Resin columns (following Harris et al., 2015), with those samples subdivided before digestion combined into a single separated Sr sample for analysis. Total combined blanks of the process were < 350 pg. Strontium isotopic compositions were analysed using a ThermoFisher Scientific TritonPlus Thermal Ionisation Mass Spectrometer (TIMS) at NOCS. Standard NBS987 was measured as an external standard. The mean value of NBS987 (n = 26) throughout the analytical period was $^{87}Sr/^{86}Sr = 0.710243 \pm 0.000024$ (2σ). Internal precision was monitored by measuring 150 ratios per sample and the error of each analysis is reported as 2 standard errors (±2 SE). Calcium mapping was undertaken at NOCS using a Carl Zeiss Leo1450VP Scanning Electron Microscope (SEM) coupled to an Oxford Instruments Energy Dispersive X-ray Spectroscopy (EDS) X-act-10 mm^2 silicon drift detector utilising the Aztec energy software. Typical SEM operation conditions were 20 kV at a working distance of 19 mm.

4. Results

Here, we present new major and trace element concentrations and radiogenic strontium isotope analyses of bulk whole rock powders and progressive leaching steps: (i) an initial leaching step using 10 % acetic acid; (ii) an intermediate step using 3 M HCl; (iii) and final dissolution of the remaining rock residue using a standard HF and HNO_3 digest (Fig. 2). Additional analyses of serpentine and chrysotile veins, serpentinite breccias, cohesive fault gouges, and gabbros complement the progressive leaching analyses of bulk rock powders (see supplementary materials).

4.1. Strontium concentrations and radiogenic isotopes

$^{87}Sr/^{86}Sr$ whole rock values in samples from the Olympus Diapir fall into a wide range between 0.7053 and 0.7091 (Fig. 3; Fig. 8). These values are significantly higher than the proposed mantle values for the Troodos ophiolite based on analyses of fresh volcanic glasses (0.7033 to 0.7042; Rautenschlein et al., 1985). Leachates (10 % acetic and 3 M HCl) and rock residue $^{87}Sr/^{86}Sr$ analyses from Olympus Diapir samples are similar to the corresponding whole rock values (Fig. 3; Fig. 8). More strongly serpentinized Olympus Diapir samples have more radiogenic $^{87}Sr/^{86}Sr$ values and lower Sr concentrations (Fig. 3). Each leaching step and rock residue generally yield similar Sr concentrations (Fig. 8b; as shown by near horizontal connecting lines between each respective step).

$^{87}Sr/^{86}Sr$ values of whole rock bulk powders from the Artemis Diapir also display a wide range between 0.7053 and 0.7085 (Fig. 8). However, in contrast to the Olympus Diapir samples, $^{87}Sr/^{86}Sr$ analyses of leachates and rock residues from the Artemis Diapir are different from the corresponding whole rock (Fig. 4; Fig. 5; Fig. 8). The relatively easily mobilised 10 % acetic acid leachates of the Artemis Diapir fall into two discrete groups: (1) Two samples (AR2, Fig. 4; AO2) yield strontium isotopic compositions between 0.7053 and 0.7056. These values are similar to the $^{87}Sr/^{86}Sr$ ratios of Troodos hyperalkaline (up to pH 13) Troodos groundwaters (Evans et al., 2024a); and (2) 8 samples that range between 0.7086 and 0.7088 (Table S2; Fig. 4, Fig. 5; Fig. 10). For both groups, the $^{87}Sr/^{86}Sr$ analyses of the 3 M HCl leachate are similar to the corresponding whole rock value (Fig. 4, Fig. 5; Fig. 8). The final rock $^{87}Sr/^{86}Sr$ residues of the Artemis Diapir yield relatively low strontium isotopic compositions, falling into two discrete groups: (1) 8 samples yield relatively low Sr isotope ratios between 0.7053 and 0.7063 whereas (2) 2 samples yield $^{87}Sr/^{86}Sr$ values between 0.7072 and 0.7080 (Fig. 4, Fig. 5; Fig. 8). These differences between whole rock and

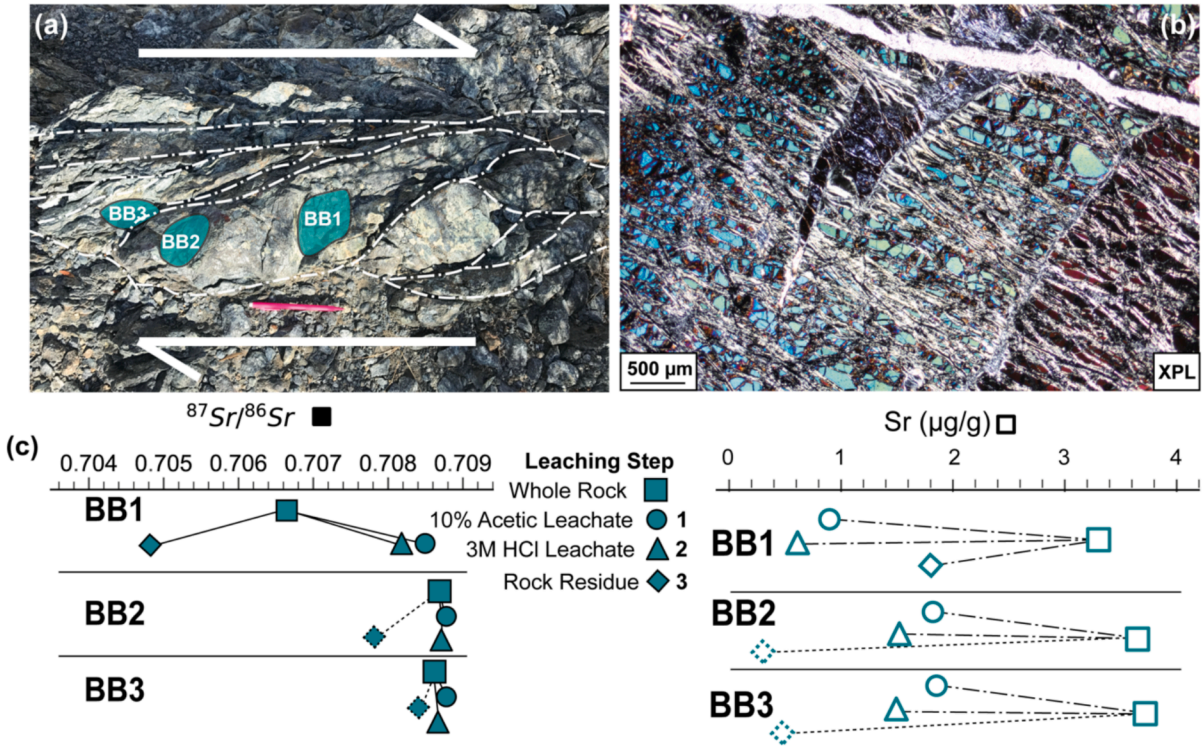

Fig. 7. (a) Sub-vertical dextral serpentinite shear zone within the Limassol Forest Complex. Partly serpentinized sample BB1 located in core of a clast hosted within the serpentinite shear zone. Completely serpentinized sample BB2 is from the margin of the shear zone. Completely serpentinized sample BB3 is located in the serpentinite matrix. Dashed-dotted white lines show complex array of shear planes. (b) Cross-polarised light (XPL) photomicrograph of sample BB1 showing partly serpentinized mesh textured serpentine with a strong fabric. (c) Plots of $^{87}Sr/^{86}Sr$ and Sr (µg/g) of each progressive leaching step and whole rocks. Samples BB2 and BB3 Rock Residues were calculated from mass balance and are shown by dotted edges and connecting lines.

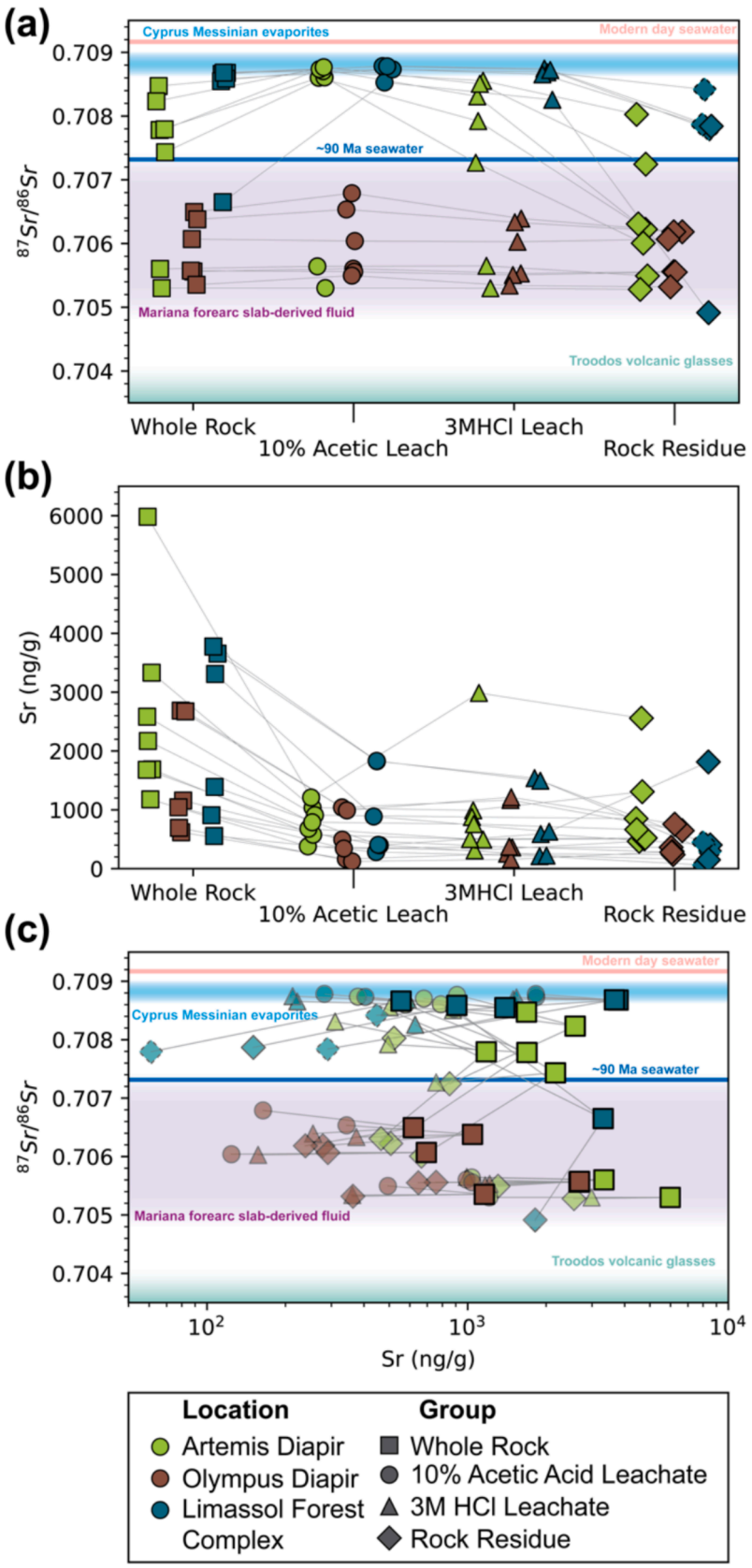

Fig. 8. (a) $^{87}Sr/^{86}Sr$ plot of whole rocks and progressive leaching steps show variations of each sample at each respective step. Grey lines show connecting progressive leaching steps. $^{87}Sr/^{86}Sr$ signatures of modern and Cretaceous seawater (~90 Ma) from (McArthur et al., 2012), Troodos volcanic glasses, (Rautenschlein et al., 1985), Mariana slab-derived fluids, (Mottl et al., 2004, 2023; Bickford et al., 2008), and Cyprus Messinian evaporites (Schildgen et al., 2014). Dashed edges show values determined from mass balance. (b) Plot of Sr (ng/g) concentration of leaching steps showing similar Sr concentrations between each respective step. (c) $^{87}Sr/^{86}Sr$ plotted against Sr (ng/g) of each respective leaching step. Grey lines connect each leaching step to the corresponding whole rock.

respective leachate analyses reflect textural differences visible in outcrop (Fig. 4; Fig. 5). For example, locality AR shows the core (AR2) of a completely serpentinized clast of the Artemis Diapir preserving similar $^{87}Sr/^{86}Sr$ whole rock (0.7056) and leachate ratios (0.7055–57) (Fig. 4). In contrast, the rim of this block (AR1) yields relatively radiogenic whole rock signatures (0.7078) (Fig. 4) with an initial radiogenic 10 % acetic leachate of 0.7086, a secondary 3 M HCl leachate of 0.7079. Only the residue analysis yields more primitive rock residue ($^{87}Sr/^{86}Sr$ ~0.7062; Fig. 4). Differences between the $^{87}Sr/^{86}Sr$ ratios of the core and rim of the completely serpentinized blocks and clasts of the Artemis Diapir do not occur in every clast of the Artemis Diapir. For example, subdivision and leaching treatment of rock and vein samples from Artemis Diapir rock CU show a consistent acetic leachate signature of $^{87}Sr/^{86}Sr$ ~0.7086 similar to Messinian seawater. A relatively oxidized zone (CU1), background zone (CU4) and alteration halo (CU2) around a fibrous chrysotile vein (CU3) all have relatively radiogenic whole rocks ($^{87}Sr/^{86}Sr$ ~0.7075), but strong leaching reveals a relatively primitive ($^{87}Sr/^{86}Sr$ ~0.7055 to 0.7060) residue. The chrysolite vein has a low Sr concentration (0.6 μg/g) and $^{87}Sr/^{86}Sr$ ~0.7076, noticeably lower than the acetic acid leachates. Serpentine vein (CU5) yields a radiogenic signal ($^{87}Sr/^{86}Sr = 0.7084$) similar to the streams and rivers draining the Troodos Mantle sequence (Evans et al., 2024a), and is higher than the chrysotile vein and nearby whole rock samples (Fig. 5).

In contrast to the Troodos Mantle Sequence, whole rock $^{87}Sr/^{86}Sr$ values from the Limassol Forest Complex display a narrow range between 0.70855 and 0.70868 (Fig. 8) except for a single sample (BB1) with $^{87}Sr/^{86}Sr$ ~0.7066, which is a partly serpentinized clast hosted in a dextral serpentinite scaly-phyllonitic shear zone (Fig. 7). The rock residue from the core of the shear zone (BB1) has a relatively primitive $^{87}Sr/^{86}Sr$ of 0.7049. 10 % acetic acid leachates from the Limassol Forest Complex predominantly fall into a narrow range (0.7087 to 0.7088) (Fig. 7; Fig. 8). The rock residue of another LFC sample (BD1) has a relatively more radiogenic Sr isotope composition of 0.7079 than sample BB1 from the core of a shear zone. Limassol Forest Complex 3 M HCl leachates show a narrow range ($^{87}Sr/^{86}Sr$ ~0.7082 to 0.7087; Fig. 7; Fig. 8). Strongly serpentinized Samples BB2 and BB3 had 90 % of their whole rock Sr concentration leached by 10 % acetic acid and 3 M HCl leachates (Fig. 7; Table S2, S3).

4.2. Major element leaching concentrations

Magnesium concentrations between respective 10 % acetic acid leachates, 3 M HCl leachates, and rock residues are significantly different irrespective of geological domain (Fig. 9a). The 10 % acetic acid leachates Mg concentrations are generally < 2.5 wt%. 10 % acetic acid samples with lower $^{87}Sr/^{86}Sr$ ratios (0.7053 to 0.7068) yield higher Mg wt.% concentrations (>1 to < 2.5 wt%) when compared to samples with higher $^{87}Sr/^{86}Sr$ ratios (0.70865 to 0.7088) (Fig. 9a). In contrast, the 3 M HCl leachates of each domain yield significantly higher Mg concentrations (>4 wt%; Fig. 9a). The 3 M HCl leachates generally fall between respective 10 % acetic leachates and rock residues (Fig. 9a). The rock residues generally yield the highest Mg concentrations of up to 17.6 wt% (Fig. 9a) reflecting the dissolution of serpentine and minor primary phases if present.

Similarly, Fe concentrations vary significantly between respective leaching steps (Fig. 9b) and are similar irrespective of geological domain. The 10 % acetic acid leachates yield Fe concentrations of < 0.8 wt% (Table S2) and are generally lower than corresponding 3 M HCl leachates and rock residues. The 3 M HCl leachates also generally fall between respective 10 % acetic leachates and rock residues (Fig. 9b) and rock residues show the highest Fe concentrations of up to 7 wt%.

Although some progressive leaching samples show variation in Ca concentrations between respective steps, there is greater overlap in Ca concentrations than compared to Mg and Fe (Fig. 9c) and clear differences between geological domains. The range in Ca concentrations of the 10 % acetic leachates of all domains is similar (0.01 to 0.1 wt%;

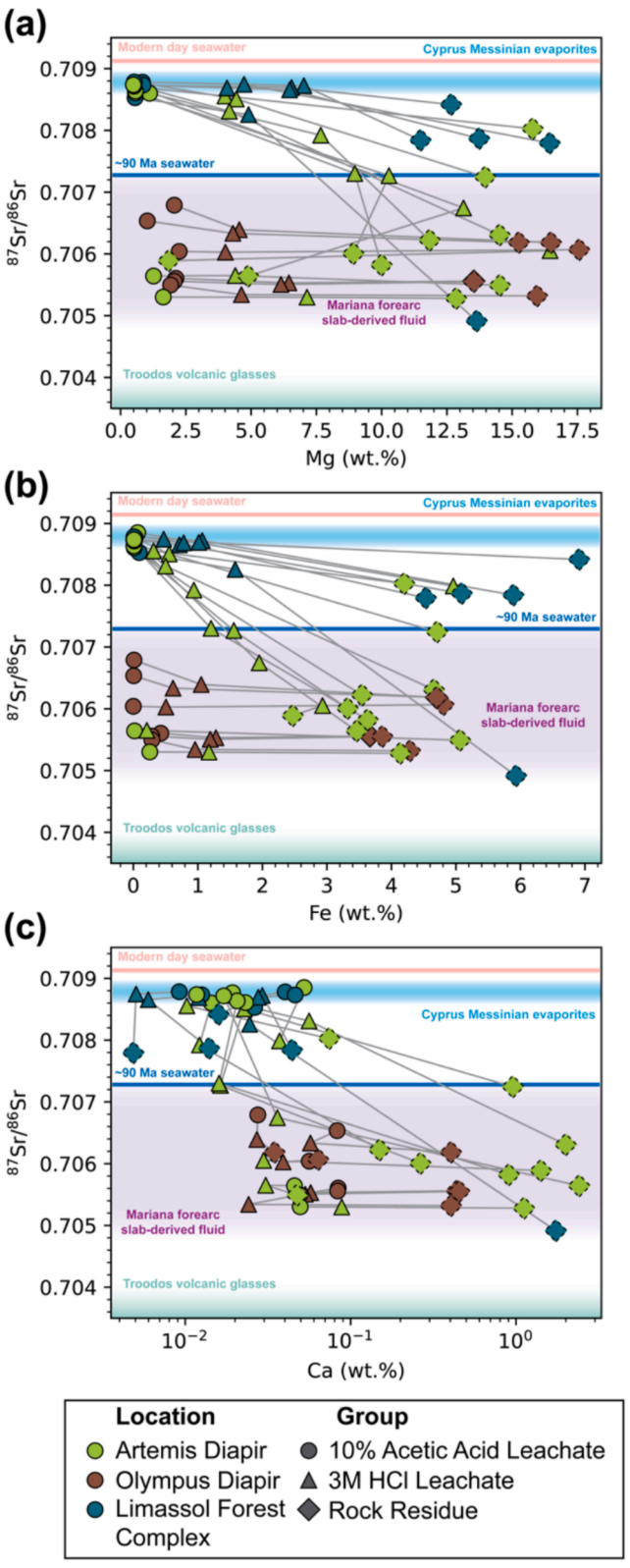

Fig. 9. (a) $^{87}Sr/^{86}Sr$ plotted against Mg (wt.%) showing each respective leaching step. (b) $^{87}Sr/^{86}Sr$ plotted against Fe (wt.%) showing each respective leaching step. (c) $^{87}Sr/^{86}Sr$ plotted against Ca (wt.%) showing each respective leaching step. Grey lines show connecting progressive leaching steps. $^{87}Sr/^{86}Sr$ signatures of modern and Cretaceous seawater (~90 Ma) from (McArthur et al., 2012), Troodos volcanic glasses, (Rautenschlein et al., 1985), Mariana slab-derived fluids, (Mottl et al., 2004, 2023; Bickford et al., 2008), and Cyprus Messinian evaporites (Schildgen et al., 2014). Dashed edges show values determined from mass balance.

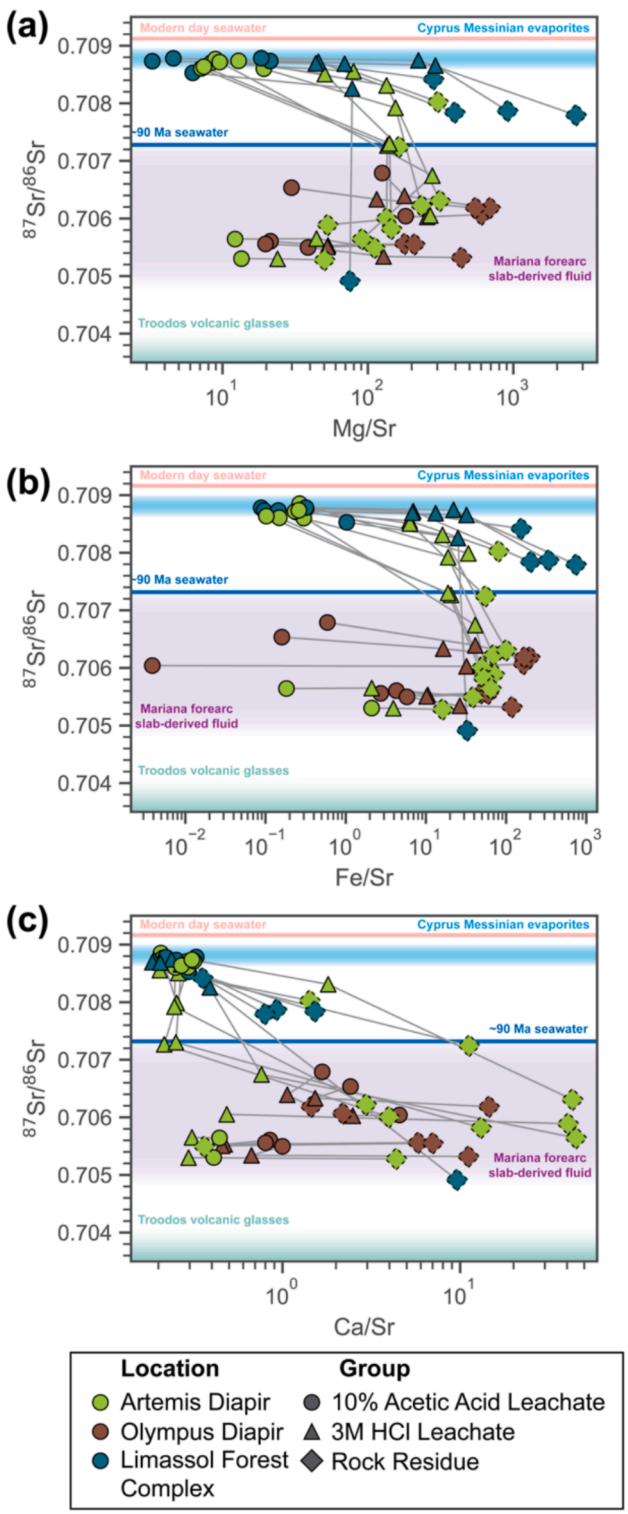

Fig. 10. $^{87}Sr/^{86}Sr$ plotted against Mg/Sr $\left(\frac{\mu g/g}{ng/g}\right)$ showing each respective leaching step. (b) $^{87}Sr/^{86}Sr$ plotted against Fe/Sr $\left(\frac{\mu g/g}{ng/g}\right)$ showing each respective leaching step. (c) $^{87}Sr/^{86}Sr$ plotted against Ca/Sr $\left(\frac{\mu g/g}{ng/g}\right)$ showing each respective leaching step. Grey lines show connecting progressive leaching steps. $^{87}Sr/^{86}Sr$ signatures of modern and Cretaceous seawater (~90 Ma) from (McArthur et al., 2012), Troodos volcanic glasses, (Rautenschlein et al., 1985), Mariana slab-derived fluids, (Mottl et al., 2004; Bickford et al., 2008; Mottl et al., 2023), and Cyprus Messinian evaporites (Schildgen et al., 2014). Dashed edges show values determined from mass balance.

Fig. 9c). The Ca concentrations of 3 M HCl step are similar to the corresponding 10 % acetic acid leachate (Fig. 9c). However, the Ca concentrations of the rock residues are generally significantly higher (up to 2.5 wt%). Rock residue samples with lower $^{87}Sr/^{86}Sr$ ratios (<0.7073) are generally offset the other respective leaching steps (Fig. 9c). Whereas the rock residues of the Limassol Forest Complex and Artemis Diapir that have high (>0.7077) $^{87}Sr/^{86}Sr$ ratios are similar to other leaching steps (Fig. 9c). However, we note that 3 samples with lower $^{87}Sr/^{86}Sr$ (>0.7053 to <0.7062) ratios also yield similar Ca concentrations to other respective leaching steps (Fig. 9c).

Normalization of major element concentration to Sr (e.g., Ca/Sr) results in similar trends (Fig. 10). However, some of the Mg/Sr of the 3 M HCl leachates and rock residues of the Artemis Diapir and sample BB1 of the Limassol Forest Complex are similar (Fig. 10a). Despite similarities in Mg/Sr ratios these samples generally yield distinct $^{87}Sr/^{86}Sr$ ratios (shown sub-vertical grey connecting lines; Fig. 10a). Whereas in all geological domains, Fe/Sr ratios generally show greater separation between respective leaching steps, but we note that 3 M HCl leachates and corresponding rock residues plot more tightly compared to 10 % acetic acid leachates (Fig. 10b). In comparison, Ca/Sr ratios are more complex than Mg/Sr and Fe/Sr respectively (Fig. 10) with different trends in each respective leaching step and between each geological domain. Despite the complexity, Ca/Sr of rock residues are generally separated from corresponding 3 M HCl and 10 % acetic acid leachates (Fig. 10c). Some 3 M HCl leachates yield similar Ca/Sr as 10 % acetic acid leachates (Fig. 10c).

4.3. *Fluid-mobile trace element concentrations*

Whole rock normalized (leachates normalized to corresponding whole rock value) plots of fluid mobile element concentrations (Sr, Li, Rb, Cs, Ba; Fig. 11) show each leaching step reflects generally range between ~20 and ~40 % of the total element budget (Fig. 11). The relative proportions of each leaching step from the Olympus and Artemis diapirs and Limassol Forest Complex are generally similar at each step across fluid-mobile elements (Fig. 11). Artemis Diapir whole rock samples with Sr isotopic compositions of ~0.7053–56 yield higher concentrations of fluid-mobile trace elements (e.g., Li, Rb, Cs, Ba) than serpentinized samples within the Troodos Mantle Sequence (Fig. 12a). Each progressive leaching step shows separation in fluid-mobile trace element concentrations with rock residues generally yielding higher concentrations and 10 % acetic acid leachates having lower concentrations (Fig. 12b). The 3 M HCl leachates generally fall between 10 % acetic acid leachates and leaching residue (Fig. 12b). Normalisation of fluid-mobile trace elements to Sr (i.e., $\Sigma Rb + Cs + Li + Ba)/Sr$) results in similar trends (Fig. 12c).

Chrysotile veins within the Artemis Diapir yield high concentrations of fluid mobile elements (Table S1). For example, Na concentrations of the chrysotile separates range from 13 to 2331 μg/g, nearly an order of magnitude higher than whole rocks (Table S2). 10 % acetic acid leachates of the chrysotile veins yield Na concentrations ranging from 4 to 2837 μg/g.

5. Discussion

5.1. *Leaching systematics*

Progressive chemical leaching is an imprecise approach and inevitably leads to some mixing of signatures. However, our progressive leaching steps do show significantly different major element concentrations at respective steps (Fig. 9). Based on detailed petrography, the initial 10 % acetic acid leachate was expected to predominantly mobilise trace amounts (~<5 %) of calcium carbonate (Fig. 3; Fig. 6), ±magnesite and brucite if present. The relatively high concentrations of Mg (up to 2.5 wt%) in the 10 % acetic acid leachates is likely the result of the dissolution of predominantly brucite with minor magnesite and

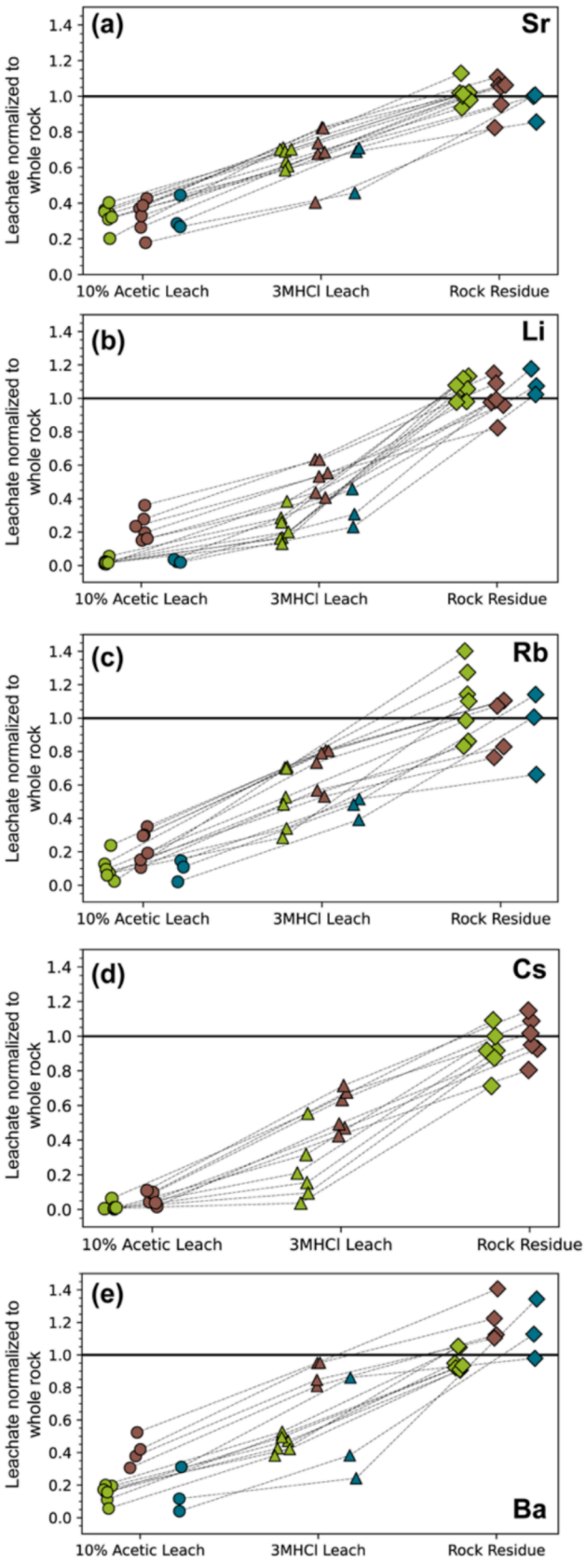

(caption on next column)

Fig. 11. Cumulative plots of each leaching step normalized to the corresponding whole rock value for (a) Sr, (b) Li, (c) Rb, (d) Cs, (e) Ba. The mean mass balance error of all elements is <±10 % and the 1σ mass balance error of all elements is <±20 % (see Table S8; individual mass balance errors of some samples of Rb and Ba are up to ± 40 %) of the whole rock value showing good recovery in the progressive leaching methodology. Brown refers to the Olympus Diapir, green refers to the Artemis Diapir, and teal refers to the Limassol Forest Complex. Circles refer to 10 % acetic acid leachates, triangles refer to 3 M HCl leachates, and diamonds refer to the rock residue. We note that sample AH2 Ba rock residue concentration analysis is an outlier and is not plotted.

perhaps dolomite. Although not detected in thin sections or by SEM-EDS, brucite likely occurs in trace amounts (~<5%) within Troodos serpentinized rocks. Brucite may be mobilised during thin section preparation, resulting in the lack of petrographically identified brucite, but should be identified in XRD analyses. In some samples of the Olympus Diapir, open space associated with olivine-serpentine grain boundaries (Evans et al., 2021) may result from the dissolution of brucite.

The application of 10 % acetic acid to decarbonate rock samples is routine (e.g., Jewell et al., 2022) and has previously also been applied to decarbonate serpentinized mantle peridotites (Hostetler et al., 1966; Snow et al., 1993; Bickford et al., 2008; Harvey et al., 2014; Nielsen et al., 2024). In addition to dissolving carbonate and other easily mobile fractions such as hydroxides, recent work has shown 10 % acetic acid can also dissolve trace amounts ~4 % of serpentine (Nielsen et al., 2024). The Fe mobilised during the initial 10 % acetic acid leaching could be sourced from iron hydroxides minerals such as pyroaurite or Fe-brucite (e.g., Hostetler et al., 1966; Klein et al., 2009; Templeton and Ellison, 2020). Secondary andradite is unlikely to be the source of Fe during the initial 10 % acetic acid leaching due to the similar initial leaching Fe concentrations between the Olympus (no observed andradite) and Artemis Diapir.

As anticipated, Mg and Fe concentrations in 3 M HCl leachates indicate that serpentine is being gently attacked, with 33 ± 18 % (1σ, n = 22; Table S7) of the total Mg mobilised during this step. Whereas 18 ± 11 % (1σ, n = 22; Table S7) of the total Fe budget was mobilised during 3 M HCl leaching. This demonstrates the inherent non-uniformity of leaching experiments and individual elements yield differing leaching systematics. The remaining Mg and Fe budgets within the rock residues (Table S7) are consistent with the dissolution of serpentine and (where applicable) primary mantle minerals such as olivine and orthopyroxene.

Similarly, the majority of the Ca budget resides in the rock residue (71 ± 27 %; 1σ, n = 22; Table S7) with a relatively small fraction occurring in the initial 10 % acetic acid leachate (17 ± 17 %; 1σ, n = 23; Table S7). SEM-EDS mapping (Fig. 6) reveals acicular inclusions of trace calcium carbonate within chrysotile veins, serpentine veins, and the wall rock (Fig. 6). These inclusions are likely dissolved during the initial 10 % acetic acid leach, imparting a distinctive $^{87}Sr/^{86}Sr$ of the carbonate to the initial leachates. Recent in situ Ca abundance mapping via laser ablation mass spectrometry (Evans et al., 2024b), together with SEM-EDS mapping (Fig. 6c), confirms the occurrence of andradite as a relatively high calcium phase, in addition to calcium carbonate in these rocks. In serpentine, relatively high amounts of Ca occur and its abundance varies significantly depending on serpentine phase (e.g., low Ca in serpentine veins; Evans et al., 2024b). Consequently, variations in whole rock Ca concentrations (Table S7) are likely controlled not only by the abundance of trace calcium carbonate but also andradite and the extent of high Ca serpentine phases. Since acetic acid leaching removes carbonate phases, the high Ca concentrations remaining in rock residues indicate that serpentine and andradite host most of the Ca budget in both the Troodos Mantle Sequence and Limassol Forest Complex. This suggests that Ca in serpentine and andradite is relatively more robust to 10 % acetic acid and 3 M HCl leaching procedures than Mg and Fe.

Major element (Mg, Fe, Ca) leaching systematics are consistent with 10 % acetic acid leachates reflecting the dissolution of easily mobile

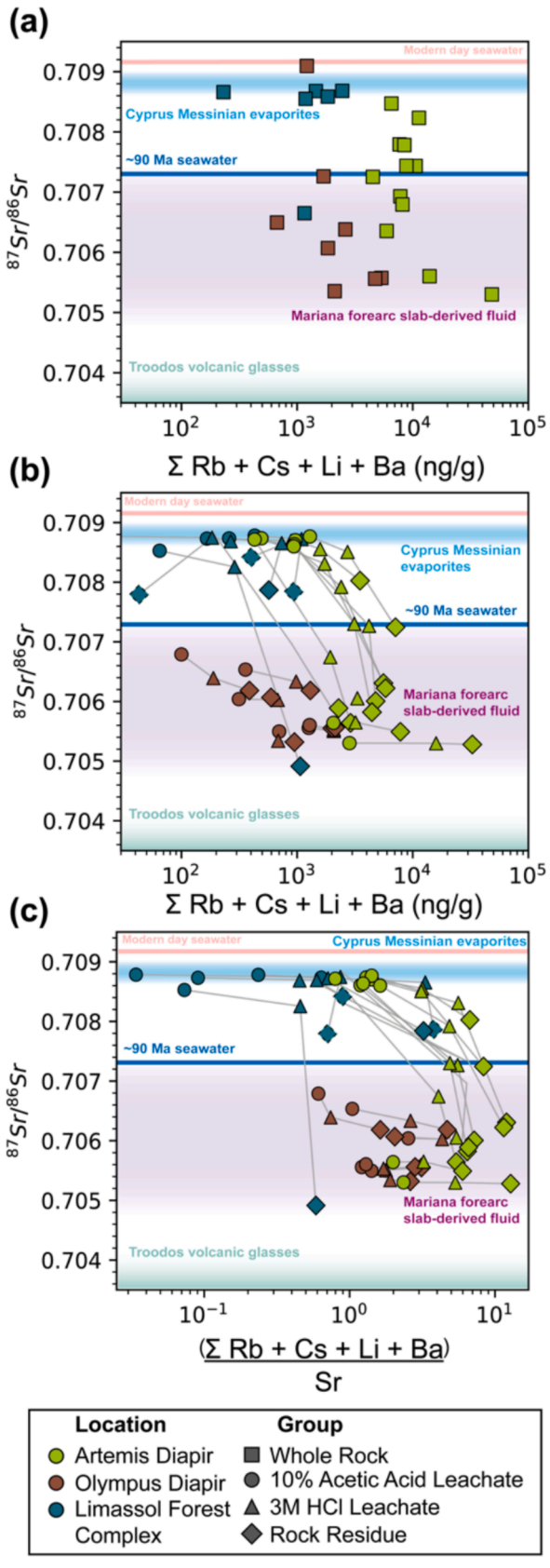

(caption on next column)

Fig. 12. (a) Plot of whole rock $^{87}Sr/^{86}Sr$ against the sum of fluid mobile element concentrations (ng/g; defined here as Li, Rb, Cs, Ba). (b) Plot of leachate and rock residue$^{87}Sr/^{86}Sr$ against the sum of fluid mobile element concentrations. (c) Plot of leachate and rock residue$^{87}Sr/^{86}Sr$ against the sum of fluid mobile element concentrations over Sr concentration (all ng/g). Grey lines show connecting progressive leaching steps. $^{87}Sr/^{86}Sr$ signatures of modern and Cretaceous seawater (~90 Ma) from (McArthur et al., 2012), Troodos volcanic glasses, (Rautenschlein et al., 1985), Mariana slab-derived fluids, (Mottl et al., 2004, 2023; Bickford et al., 2008), and Cyprus Messinian evaporites (Schildgen et al., 2014). Dashed edges show values determined from mass balance.

fractions such as carbonates and hydroxides. In contrast, the 3 M HCl leachates reflect the partial dissolution of serpentine and the rock residues predominantly reflect the remaining serpentine. However, in contrast to major elements, Sr concentrations are similar in each leaching step (Fig. 8b; Fig. 11a; Table S6), distinct $^{87}Sr/^{86}Sr$ signatures (Fig. 8) are being recorded by the respective leachates and rock residues across differing geological domains. As a result, despite the inherent complexities and variabilities in leaching, our results demonstrate that contrasting geochemical signatures are being isolated from samples during our progressive chemical attack.

5.2. Contrasting leachate signatures

5.2.1. Troodos Mantle Sequence

Progressive leaching experiments of partly serpentinized Olympus Diapir samples yield consistent isotopic signatures across all leaching steps and whole-rock textures (Fig. 3; Fig. 8). In contrast, completely serpentinized samples from the Artemis Diapir typically produce variable isotopic signatures at each step, (Fig. 4; Fig. 5; Fig. 8), except for two more primitive (~0.705) samples (AO2, AR2; Fig. 4).

Artemis Diapir whole rocks and leachates reveal two distinct Sr isotopic endmembers: (i) a radiogenic ~0.7087 signature and (ii) a more primitive ~0.705 signature (Fig. 8). This primitive $^{87}Sr/^{86}Sr$ signature of ~0.705 in the completely serpentinized mantle rocks of the Artemis Diapir suggests that the unaltered supra-subduction-zone-related Troodos mantle $^{87}Sr/^{86}Sr$ (0.7033 to 0.7042; Rautenschlein et al., 1985) has been contaminated by subsequent fluid-rock interactions. The similar ~0.705 $^{87}Sr/^{86}Sr$ signatures and leaching patterns in both the completely serpentinized Artemis Diapir and strongly serpentinized Olympus Diapir suggests that Olympus' unaltered mantle $^{87}Sr/^{86}Sr$ ratios were likewise overprinted, even though primary mantle minerals such as olivine and orthopyroxene endure. Thus, the ~0.705 $^{87}Sr/^{86}Sr$ ratios in the Troodos Mantle Sequence likely do not reflect simple mixing between a primitive mantle endmember (0.7037; e.g., cumulate ultramafic wehrlite sample PP4; Table S1) and a more radiogenic endmember.

The $^{87}Sr/^{86}Sr$ ~0.705 signature is consistent with a source derived from a fluid generated by dehydration reactions of subducting altered ocean crust with a likely minor sediment component (Evans et al., 2024a, b). For example, this ~0.705 signature matches analyses of serpentinized peridotites and high salinity slab-derived pore waters recovered from the Mariana forearc mud volcanoes (Mottl et al., 2004, 2023; Bickford et al., 2008; Hulme et al., 2010). Previous in situ elemental mapping, stable boron isotopic compositions, and oxygen and hydrogen isotope analyses are consistent with serpentinization of the Troodos Mantle Sequence by fluids sourced from the downgoing Cyprus slab (Heaton, 1976; Sheppard, 1980; Evans et al., 2021, 2024b). Hyperalkaline (up to pH 13) meteoric-derived waters from the Artemis Diapir, with $^{87}Sr/^{86}Sr$ ratios of ~0.705, match the signatures of serpentinized Olympus and Artemis rocks (Evans et al., 2024a). It is interpreted that these meteoric groundwater signatures reflect the near surface remobilisation of strontium ultimately sourced from the dehydration of the Cyprus slab and mechanically advected to the near-surface (Evans et al., 2024a, b).

In contrast, the radiogenic $^{87}Sr/^{86}Sr$ ~0.70860 to 0.70885 signature

point to exchange with a source such as Miocene seawater (18 to 11 Ma; McArthur et al., 2012), or more specifically a Messinian seawater signature (0.7086 to 0.7089; Schildgen et al., 2014). Previous Troodos Mantle Sequence stable oxygen and hydrogen isotopic analyses are consistent with exchange with meteoric waters at temperatures < 50 °C but are inconsistent with low temperature < 50 °C seawater infiltration (Magaritz and Taylor, 1974; Heaton, 1976; Sheppard, 1980; Evans et al., 2021). In addition, previous boron isotopic analyses and in situ elemental mapping are also illuminate evidence of leaching and remobilisation of B by meteoric groundwaters resulting in low B serpentinites (Evans et al., 2024b). As a result, this radiogenic $^{87}Sr/^{86}Sr$ signatures likely mostly reflects the precipitation of trace amounts of calcium carbonate within the serpentinized peridotites from meteoric waters that had traversed the formerly overlying Messinian evaporites.

Rivers and streams draining the Troodos Mantle Sequence also yield radiogenic Sr isotope signatures between 0.7084 and 0.7086 (Evans et al., 2024a). This likely involves mixing of the ~0.7087 signature with only a minor contribution of the ~0.705 endmember, and ultimately sourced from the mobile components of the Troodos Mantle Sequence rocks, which are reflected in the easily mobilized 10 % acetic acid leachates. These relatively easily mobile portions are likely dominated by calcium carbonate occurring in discrete veins, commonly hosted within serpentine fibres of chrysotile veins (Fig. 6). The radiogenic ~0.7087 signature is not limited to the easily mobile fraction but also contributes to the 3 M HCl leachate and rock residues of both the Artemis and Olympus diapirs (Fig. 12).

5.2.2. Limassol Forest Complex

Despite geological evidence for seafloor serpentinization during tectonic and magmatic activity relating to the Arakapas transform fault (e.g., Murton, 1986; MacLeod, 1988; MacLeod et al., 1990; MacLeod and Murton, 1993; Martin et al., 2023), contrary to expectations, the Limassol Forest Complex serpentinites analysed, do not yield $^{87}Sr/^{86}Sr$ ratios similar to ~90 Ma Cretaceous seawater (~0.7073; McArthur et al., 2012).

Progressive leaching of the partly serpentinized sample BB1 (Fig. 7) reveals an easily mobilized, radiogenic signature (0.7085) and a more primitive signature (0.7049) in the residue. This relatively primitive signal could reflect a mixed source between Cretaceous seawater (~0.7073) and unaltered mantle (~<0.7037; Rautenschlein et al., 1985), which would be consistent with field observations of ultramafic and mafic dikes intruding previously serpentinized mantle peridotite. However, for sample BB1, sequential gentle acetic then 3 M HCl leaching recovered radiogenic $^{87}Sr/^{86}Sr$ (0.7083–85) values suggesting that the 0.7049 residue signal likely reflects mixing between this radiogenic (0.7083–85) and unaltered mantle source (Fig. 7, Fig. 8). In addition, most whole rock samples from the Limassol Forest Complex yield a radiogenic signature (~0.7085–87; Fig. 8) rather than the anticipated more primitive signature (~0.7073; McArthur et al., 2012) consistent with Cretaceous seawater.

An alternative source for the more primitive ~0.7049 signature reflected in the rock residue of sample BB1 is the dehydrating Cyprus slab, in a similar manner as interpreted for the Troodos Mantle Sequence rocks, given the LFC's proximity to the Cyprus trench (Fig. 1a) but this interpretation is not supported by the geology. The Troodos Mantle Sequence is characterised by its unique, eroded anticlinal domal geometry that results in its unusual outcrop pattern (Fig. 1), which does not occur in the Limassol Forest Complex. In addition, a large (80 to 120 mGal) negative Bouguer gravity anomaly is centred over the Troodos Mantle Sequence, extending to 11 km in depth (Gass and Masson-Smith, 1963; Shelton, 1993; Evans et al., 2021), similar to the inferred depth of the Cyprus slab below Mount Olympus (Mackenzie et al., 2006; Feld et al., 2017; Evans et al., 2021). In contrast, no such negative gravity anomaly occurs in the Limassol Forest Complex. Thus, pervasive serpentinization by slab-derived fluids, similar to that in the Troodos massif, is unlikely in the Limassol Forest Complex.

Although the range in the easily mobilised $^{87}Sr/^{86}Sr$ leachate signature of the Limassol Forest Complex (0.70873 to 0.70878, n = 5; Fig. 8) is bound more tightly compared to the wider range of Sr-isotopic signatures (0.7086 to 070885) yielded by gentle leaching of the Troodos Mantle Sequence rocks, both signatures are similar. This tightly constrained 0.70873 to 0.70878 value is consistent with mid-Miocene (16.2 to 15 Ma) seawater (McArthur et al., 2012) and Cyprus Messinian evaporites (Schildgen et al., 2014). Consequently, because these signatures overlap in Sr isotope space (McArthur et al., 2012; Schildgen et al., 2014; Manzi et al., 2016), it is difficult without additional isotopic evidence (e.g., O, H, and B stable isotopes) to determine if the ~0.7087 endmember in the Limassol Forest Complex reflects Miocene seawater infiltration or meteoric waters that interacted with Messinian evaporites.

5.3. Contrasting alteration histories

Progressive leaching experiments reveal distinct isotopic signatures in the Troodos Mantle Sequence and the Limassol Forest Complex. A geological model for the serpentinization of the Troodos Mantle Sequence has been recently proposed based on geochemical and isotopic signatures in river and stream waters and hyperalkaline (up to pH 13) saline groundwaters emanating from the Troodos Mantle Sequence (Evans et al., 2024a). The results from our progressive leaching experiments of Artemis and Olympus rocks are consistent with this proposed geological model of an initial pervasive serpentinization event with a fluid sourced from dehydration reactions of predominantly subducting altered ocean crust with a minor sediment component (Evans et al., 2024a, b). Focusing of these fluids due to the collision of the Eratosthenes plateau with the Cyprean trench (Robertson, 1998b, c; Evans et al., 2021) beneath the Mount Olympus region resulted in significant isostatic uplift and serpentinite diapirism (Gass and Masson-Smith, 1963; Moores and Vine, 1971; Robertson, 1977, 1998b; Evans et al., 2021), mechanically advecting these slab-derived geochemical signatures to the surface (Evans et al., 2024a, b). Continued serpentinization by slab-derived fluids from below were supplemented by the inevitable infiltration of meteoric water into the uplifting Troodos mountains (Evans et al., 2021, 2024a, b). As these meteoric waters traversed small, isolated, and irregular Messinian evaporite basins (Stow et al., 1995; Rouchy et al., 2001; Manzi et al., 2016) they channelled Messinian signatures into the underlying Troodos Mantle Sequence (Evans et al., 2024a). Such a model is consistent with previous Troodos Mantle Sequence stable oxygen and hydrogen isotope data that show exchange with meteoric water at low temperatures of < 50 °C (Magaritz and Taylor, 1974; Nuriel et al., 2009; Evans et al., 2021).

In contrast, samples from the Limassol Forest Complex are dominated by a radiogenic (~0.7087) $^{87}Sr/^{86}Sr$ signature. Our favoured interpretation is that this signature is a result of mid-Miocene seawater infiltrating the ultramafic sequences of the Limassol Forest Complex. This is because the timing of this mid-Miocene (16.2 to 15 Ma; McArthur et al., 2012) infiltration is broadly coeval with significant focussed uplift of the Limassol Forest Complex (Robertson, 1977). A consequence of this mid-Miocene seawater infiltration is serpentinization-induced isostatic uplift and concomitant volume expansion that likely contributed to the uplift of the Limassol Forest Complex (Robertson, 1977; Evans et al., 2021). The similarity in the age of seawater infiltration and mid-Miocene uplift of the Limassol Forest Complex highlights the inevitably of serpentinization-induced uplift, if pervasive serpentinization occurs. However, since the Limassol Forest Complex lacks: (i) a negative Bouguer gravity anomaly, and (ii) a domal sub-circular outcrop pattern, it is unlikely that serpentinite diapirism has occurred in a manner akin to the Troodos massif (Evans et al., 2021).

Mid-Miocene seawater infiltration would have likely been facilitated because ultramafic rocks there were not covered by a full Penrose ocean crustal sequence (Murton, 1986; MacLeod et al., 1990; Gass et al., 1994; Cox et al., 2021) as was the main part of the Troodos ophiolite. Later,

subsequent Miocene seawater and meteoric waters would have traversed formerly overlying sediments, scavenging radiogenic and fluid-mobile element geochemical signatures prior to exchange with underlying mantle peridotites. As focussed uplift of the Limassol Forest Complex persisted until the Pliocene (Robertson, 1977), serpentinization of the Limassol Forest Complex may have also endured.

5.4. Poorly soluble inclusions?

Hyperalkaline waters (up to pH 13) with very high salinities (25 to 30 % seawater total dissolved loads) and high fluid mobile element concentrations (Na, K, Li, B, Rb, Cs, Ba) emanate from rare springs in the Artemis diapir (Evans et al., 2024a). To explain the high salinities and fluid mobile element compositions of these Troodos groundwaters, it is proposed that poorly soluble inclusions weakly bound to serpentine are present in these rocks, and that these inclusions have been exposed to fluid leaching by the multiple generations of serpentine deformation and re-precipitation experienced by the Artemis Diapir serpentinites (Evans et al., 2024a). Our analyses of chrysotile veins yield variable fluid mobile trace element concentrations spanning up to three orders of magnitude (Table S1; Table S2). The mobilisation and recovery of high concentrations of Na, Li, K, Rb, Cs during the 10 % acetic acid leachate step suggest that some poorly soluble inclusions are being mobilised from the chrysotile veins, contributing to the geochemical composition of Troodos groundwaters. Analysed chrysotile veins generally have $^{87}Sr/^{86}Sr$ ratios similar to whole rocks (Fig. 5) but some serpentine veins, such as sample CU5, yield a bulk $^{87}Sr/^{86}Sr$ of 0.7084, similar to $^{87}Sr/^{86}Sr$ ratios of the streams (0.7084–86) emanating from the Troodos Mantle Sequence. The similarity in $^{87}Sr/^{86}Sr$ between Troodos mantle streams and some serpentine veins suggests complex serpentine dissolution, precipitation, and recrystallization (Fig. 5) mechanisms are ongoing in the modern meteoric-water regime with the apparent preservation of refractory signatures from preceding alteration episodes (e.g., sample AR2, ~0.705; Fig. 4).

5.5. Implications of progressive leaching experiments

Although previous studies have applied leaching techniques to serpentinized mantle peridotites, these studies have previously either: (i) only been applied to a limited number of samples (Snow et al., 1993; Bickford et al., 2008; Harvey et al., 2014; Frisby et al., 2016; Nielsen et al., 2024); (ii) limited to an acetic acid leaching step (Hostetler et al., 1966); (iii) or were limited to only one element and isotope system (Bickford et al., 2008; Harvey et al., 2014).

Despite variations and inherent complexities in the leaching systematics of different elements, our results demonstrate that distinct Sr isotopic signatures are isolated. Consequently, progressive leaching experiments can reveal different signatures between samples, geological domains, and respective leaching steps. Future studies should focus on applying multiple isotopic systems (e.g., $^{87}Sr/^{86}Sr$, Mg, Li) within a progressive leaching framework that also includes quantitative X-ray diffraction (XRD) analyses of whole rocks and rock residues. This will require much larger samples to be digested and processed.

The key implication of our results is that whole rock analyses of serpentinized mantle rocks reflect the cumulative sum of multiple alteration events, and that progressive leaching facilitates the isolation of distinct isotopic signatures that enables isotopic fingerprinting of discrete serpentinization episodes. Such an approach, especially when combined with in situ elemental and isotopic analyses (Vesin et al., 2023; Evans et al., 2024b) may ultimately permit the relative contribution of discrete serpentinization events to be quantified and placed in context within the Earth system.

6. Conclusions

(1) The application of a three-step leaching process comprising: (i) a gentle 10 % acetic acid leachate, (ii) a 3 M HCl leachate, and (iii) the HF-HNO_3 digestion of the residue isolates distinct signatures from serpentinized peridotite whole rock samples. These leaching experiments progressively liberate fluid mobile elements (such as Li, Cs, Rb, K, Na, Ba, Sr, Ca, B and U) principally due to the dissolution of carbonate, salts, and serpentine. The initial acetic acid treatment yields leachates with relatively radiogenic $^{87}Sr/^{86}Sr$ values. The more aggressive 3 M HCl leaching generally returned relatively primitive $^{87}Sr/^{86}Sr$ ratios similar to the final whole rock residues. Whole rock powders from the Troodos Mantle Sequence and Limassol Forest Complex reflect the relative contributions of differing endmember $^{87}Sr/^{86}Sr$ values with the respective whole rock values being the cumulative sum of multiple alteration events.

(2) Progressive leaching of the Troodos Mantle Sequence is consistent with initial serpentinization by fluids sourced from the stalled subduction of the Cyprus slab that triggered serpentinite diapirism. The resulting unroofing of the Troodos ophiolite resulted in the inevitable infiltration of meteoric waters that mobilise Messinian evaporite signatures and contaminate the Troodos Mantle Sequence peridotites with calcium carbonate. Such an alteration history is consistent with previous stable boron, oxygen, and hydrogen isotope analyses and emanating groundwaters.

(3) Field observations within the Limassol Forest Complex are consistent with serpentinization occurring on the Cretaceous seafloor. However, most samples yield radiogenic $^{87}Sr/^{86}Sr$ signatures from progressive leaching analyses corresponding with mid-Miocene seawater and is broadly coeval with inferred mid-Miocene uplift of the Limassol Forest Complex. Evidence from progressive leaching experiments of pervasive serpentinization by Cretaceous seawater is not forthcoming.

(4) Initial leaching of chrysotile veins within the Artemis Diapir recover high concentrations of Na, Li, K, Rb, and Cs. The mobilisation of these inclusions by meteoric water contributes to the geochemical composition of the Troodos saline hyperalkaline (up to pH 13) groundwaters. Some serpentine veins yield similar $^{87}Sr/^{86}Sr$ ratios as streams and rivers draining the Troodos Mantle Sequence, suggesting complex serpentine dissolution, precipitation, and recrystallization mechanisms are ongoing.

CRediT authorship contribution statement

Aled D. Evans: Writing – review & editing, Writing – original draft, Visualization, Validation, Resources, Project administration, Methodology, Investigation, Funding acquisition, Formal analysis, Data curation, Conceptualization. **Matthew J. Cooper:** Writing – review & editing, Resources, Methodology. **Dave Craw:** Writing – review & editing, Supervision, Conceptualization. **Damon A.H. Teagle:** Writing – review & editing, Validation, Supervision, Resources, Funding acquisition, Conceptualization.

Data availability

Data are available through Mendeley data at https://doi.org/10.17632/x8chfn6nwt.1.

Declaration of competing interest

The authors declare that they have no known competing financial interests or personal relationships that could have appeared to influence the work reported in this paper.

Acknowledgements

We thank the Geological Survey Department of the Republic of Cyprus for facilitating field work (MoU/Ref. No. 05.26.001/5). ADE acknowledges a Natural Environment Research Council-SPITFIRE CASE PhD award NE/L002531/1 (Natural History Museum CASE Partner). DAHT acknowledges a Royal Society Wolfson Research Merit Award (WM130051). We thank Dan Doran and Matt Beverly-Smith for the preparation of thick sections and Richard Pearce for assistance with the SEM. We thank Executive Editor Jeffrey Catalano and Hailiang Dong, Associate Editor Frieder Klein for editorial handling and three anonymous reviewers for their constructive comments that improved this paper.

Appendix A. Supplementary material

Supplementary tables are supplied as the following:

Table S1 – Whole rock analyses. Table S2 – 10% acetic acid leachate analyses. Table S3 – 3M HCl leachate analyses. Table S4 – Rock residue analyses. Table S5 – Accuracy and precision. Table S6 – Sr and $^{87}Sr/^{86}Sr$ mass balance. Table S7 – Major elements (Mg, Fe, Ca) mass balance. Table S8 – Fluid-mobile trace elements (Li, Rb, Cs, Ba) mass balance. Supplementary material to this article can be found online at https://doi.org/10.1016/j.gca.2025.04.001.

References

Agrinier P., Cornen G., Beslier M.-O. and Whitmarsh R. B. (1996) Mineralogical and oxygen isotopic features of serpentinites recovered from the ocean/continent transition in the Iberia Abyssal Plain. In Proc. ODP, Sci. Results, 149 (ed. Whitmarsh, R.B., Sawyer, D.S., Klaus, A., and Masson, D.G.). Ocean Drilling Program, College Station, Texas. pp. 541–552.

Albers, E., Kahl, W.-A., Beyer, L., Bach, W., 2020. Variant across-forearc compositions of slab-fluids recorded by serpentinites: Implications on the mobilization of FMEs from an active subduction zone (Mariana forearc). Lithos 364–365, 105525.

Alt, J.C., Schwarzenbach, E.M., Früh-Green, G.L., Shanks, W.C., Bernasconi, S.M., Garrido, C.J., Crispini, L., Gaggero, L., Padrón-Navarta, J.A., Marchesi, C., 2013. The role of serpentinites in cycling of carbon and sulfur: Seafloor serpentinization and subduction metamorphism. Lithos 178, 40–54.

Alt, J.C., Shanks, W.C., 2006. Stable isotope compositions of serpentinite seamounts in the Mariana forearc: Serpentinization processes, fluid sources and sulfur metasomatism. Earth Planet. Sci. Lett. 242, 272–285.

Andreani, M., Mével, C., Boullier, A.-M., Escartín, J., 2007. Dynamic control on serpentine crystallization in veins: Constraints on hydration processes in oceanic peridotites. Geochem. Geophys. Geosyst. 8.

Bach, W., Garrido, C.J., Paulick, H., Harvey, J., Rosner, M., 2004. Seawater-peridotite interactions: First insights from ODP Leg 209, MAR 15°N. Geochem. Geophys. Geosyst. 5.

Bach, W., Paulick, H., Garrido, C.J., Ildefonse, B., Meurer, W.P., Humphris, S.E., 2006. Unraveling the sequence of serpentinization reactions: petrography, mineral chemistry, and petrophysics of serpentinites from MAR 15°N (ODP Leg 209, Site 1274). Geophys. Res. Lett. 33, L13306.

Barnes, I., O'Neil, J.R., 1969. The Relationship between Fluids in Some Fresh Alpine-Type Ultramafics and Possible Modern Serpentinization, Western United States. GSA Bull. 80, 1947–1960.

Bayrakci, G., Minshull, T.A., Sawyer, D.S., Reston, T.J., Klaeschen, D., Papenberg, C., Ranero, C., Bull, J.M., Davy, R.G., Shillington, D.J., Perez-Gussinye, M., Morgan, J. K., 2016. Fault-controlled hydration of the upper mantle during continental rifting. Nat. Geosci. 9, 384–388.

Bickford, M.E., Siegel, D.I., Mottl, M.J., Hill, B.M., Shosa, J., 2008. Strontium isotopic relations among pore fluids, serpentine matrix, and harzburgite clasts, South Chamorro Seamount, Mariana forearc. Chem. Geol. 256, 24–32.

Boillot, G., Grimaud, S., Mauffret, A., Mougenot, D., Kornprobst, J., Mergoil-Daniel, J., Torrent, G., 1980. Ocean-continent boundary off the Iberian margin: A serpentinite diapir west of the Galicia Bank. Earth Planet. Sci. Lett. 48, 23–34.

Boschi, C., Dini, A., Früh-Green, G.L., Kelley, D.S., 2008. Isotopic and element exchange during serpentinization and metasomatism at the Atlantis Massif (MAR 30°N): Insights from B and Sr isotope data. Geochim. Cosmochim. Acta 72, 1801–1823.

Burkhard, D.J.M., O'Neil, J.R., 1988. Contrasting serpentinization processes in the eastern Central Alps. Contrib. Mineral. Petrol. 99, 498–506.

Coleman, R.G., Keith, T.E., 1971. A chemical study of serpentinization—Burro Mountain. California. J. Petrol. 12, 311–328.

Cooperdock, E.H.G., Stockli, D.F., 2016. Unraveling alteration histories in serpentinites and associated ultramafic rocks with magnetite (U-Th)/He geochronology. Geology 44, 967–970.

Coulton, A.J., Harper, G.D., O'Hanley, D.S., 1995. Oceanic versus emplacement age serpentinization in the Josephine ophiolite: Implications for the nature of the Moho at intermediate and slow spreading ridges. J. Geophys. Res. 100, 22245–22260.

Cox, S., Fagereng, Å., MacLeod, C.J., 2021. Shear zone development in serpentinized mantle: Implications for the strength of oceanic transform faults. J. Geophys. Res. Solid Earth 126.

Davies, Q.J., 2001. Climatic and Tectonic Controls on Deep Water Sedimentary Cyclicity: Evidence from the Miocene to Pleistocene of Cyprus. Open University, PhD.

Eaton, S., Robertson, A., 1993. The Miocene Pakhna Formation, southern Cyprus and its relationship to the Neogene tectonic evolution of the Eastern Mediterranean. Sediment. Geol. 86, 273–296.

Ergün, M., Okay, S., Sari, C., Zafer, O.E., Ash, M., Hall, J., Miller, H., 2005. Gravity anomalies of the Cyprus Arc and their tectonic implications. Mar. Geol. 221, 349–358.

Evans, A.D., Craw, D., Teagle, D.A.H., 2024a. Active near-surface mobilisation of slab-derived geochemical signatures by hyperalkaline waters in brecciated serpentinites. Chem. Geol. 643, 121822.

Evans, A.D., Standish, C.D., Milton, J.A., Robbins, A.G., Craw, D., Foster, G.L., Teagle, D. A.H., 2024b. Imaging of boron in altered mantle rocks illuminates progressive serpentinisation episodes. Geochem. Perspect. Lett. 29, 20–25.

Evans, A.D., Teagle, D.A.H., Craw, D., Henstock, T.J., Falcon-Suarez, I.H., 2021. Uplift and exposure of serpentinized massifs: Modeling differential serpentinite diapirism and exhumation of the troodos mantle sequence, Cyprus. J. Geophys. Res. Solid Earth 126, e2020JB021079.

Fagereng Å. and MacLeod C. J. (2019) Chapter 18 - On Seismicity and Structural Style of Oceanic Transform Faults: A Field Geological Perspective From the Troodos Ophiolite, Cyprus. In Transform Plate Boundaries and Fracture Zones (ed. J. C. Duarte). Elsevier. pp. 437–459.

Feld, C., Mechie, J., Hübscher, C., Hall, J., Nicolaides, S., Gurbuz, C., Bauer, K., Louden, K., Weber, M., 2017. Crustal structure of the Eratosthenes Seamount, Cyprus and S. Turkey from an amphibian wide-angle seismic profile. Tectonophysics 700–701, 32–59.

Francis, T.J.G., 1981. Serpentinization faults and their role in the tectonics of slow spreading ridges. J. Geophys. Res. 86, 11616.

Frisby, C., Bizimis, M., Mallick, S., 2016. Seawater-derived rare earth element addition to abyssal peridotites during serpentinization. Lithos 248–251, 432–454.

Früh-Green, G.L., Connolly, J.A.D., Plas, A., Kelley, D.S., Grobéty, B., 2004. Serpentinization of oceanic peridotites: implications for geochemical cycles and biological activity. The Subseafloor Biosphere at mid-Ocean Ridges 144, 119–136.

Früh-Green, G.L., Kelley, D.S., Bernasconi, S.M., Karson, J.A., Ludwig, K.A., Butterfield, D.A., Boschi, C., Proskurowski, G., 2003. 30,000 years of hydrothermal activity at the lost city vent field. Science 301, 495–498.

Früh-Green, G.L., Weissert, H., Bernoulli, D., 1990. A multiple fluid history recorded in Alpine ophiolites. J. Geol. Soc. London 147, 959–970.

Fryer, P., Ambos, E.L., Hussong, D.M., 1985. Origin and emplacement of Mariana forearc seamounts. Geology 13, 774.

Gass, I.G., 1968. Is the Troodos Massif of Cyprus a Fragment of Mesozoic Ocean Floor? Nature 220, 39–42.

Gass, I.G., 1977. Origin and emplacement of ophiolites. Geol. Soc. Lond. Spec. Publ. 7, 72–76.

Gass I. G., Macleod C. J., Murton B. J., Panayiotou A., Simonian K. O. and Xenophontos C. (1994) The geology of the Southern Troodos transform fault zone. In Memoir, vol. 9 Geological Survey Department of Cyprus, Nicosia. p. 218.

Gass, I.G., Masson-Smith, D., 1963. The Geology and Gravity Anomalies of the Troodos Massif, Cyprus. Proc. R. Soc. B Biol. Sci. 157, 587–588.

Granot, R., 2016. Palaeozoic oceanic crust preserved beneath the eastern Mediterranean. Nat. Geosci. 9, 701–705.

Harris, M., Coggon, R.M., Smith-Duque, C.E., Cooper, M.J., Milton, J.A., Teagle, D.A.H., 2015. Channelling of hydrothermal fluids during the accretion and evolution of the upper oceanic crust: Sr isotope evidence from ODP Hole 1256D. Earth Planet. Sci. Lett. 416, 56–66.

Harvey, J., Savov, I.P., Agostini, S., Cliff, R.A., Walshaw, R., 2014. Si-metasomatism in serpentinized peridotite: The effects of talc-alteration on strontium and boron isotopes in abyssal serpentinites from Hole 1268a, ODP Leg 209. Geochim. Cosmochim. Acta 126, 30–48.

Hayes, G.P., Moore, G.L., Portner, D.E., Hearne, M., Flamme, H., Furtney, M., Smoczyk, G.M., 2018. Slab2, a comprehensive subduction zone geometry model. Science 362, 58–61.

Heaton, T., 1976. Hydrogen and oxygen isotope study of the metamorphism and mineralisation of the Troodos Complex. PhD, University of Edinburgh, Cyprus.

Hostetler, P.B., Coleman, R.G., Mumpton, F.A., Evans, B.W., 1966. Brucite in alpine serpentinites. Am. Mineral. 51, 75–98.

Hulme, S.M., Wheat, C.G., Fryer, P., Mottl, M.J., 2010. Pore water chemistry of the Mariana serpentinite mud volcanoes: A window to the seismogenic zone. Geochem. Geophys. Geosyst. 11.

Hyndman, R.D., Peacock, S.M., 2003. Serpentinization of the forearc mantle. Earth Planet. Sci. Lett. 212, 417–432.

Jewell, A.M., Cooper, M.J., Milton, J.A., James, R.H., Crocker, A.J., Wilson, P.A., 2022. Chemical isolation and isotopic analysis of terrigenous sediments with emphasis on effective removal of contaminating marine phases including barite. Chem. Geol. 589, 120673.

Jochum, K.P., Nohl, U., Herwig, K., Lammel, E., Stoll, B., Hofmann, A.W., 2005. GeoReM: A new geochemical database for reference materials and isotopic standards. Geostand Geoanalyt Res 29, 333–338.

Kahl, W.-A., Jöns, N., Bach, W., Klein, F., Alt, J.C., 2015. Ultramafic clasts from the South Chamorro serpentine mud volcano reveal a polyphase serpentinization history of the Mariana forearc mantle. Lithos 227, 1–20.

Kempler, D., Ben-Avraham, Z., 1987. The tectonic evolution of the Cyprean Arc. Ann. Tecton. 1, 58–71.

Kerrick, D., 2002. Serpentinite seduction. Science 298, 1344–1345.
Klein, F., Bach, W., Jöns, N., McCollom, T., Moskowitz, B., Berquó, T., 2009. Iron partitioning and hydrogen generation during serpentinization of abyssal peridotites from 15°N on the Mid-Atlantic Ridge. Geochim. Cosmochim. Acta 73, 6868–6893.
Klein, F., Humphris, S.E., Bach, W., 2020. Brucite formation and dissolution in oceanic serpentinite. Geochem. Perspect. Lett. 16, 1–5.
Kodolányi, J., Pettke, T., 2011. Loss of trace elements from serpentinites during fluid-assisted transformation of chrysotile to antigorite — An example from Guatemala. Chem. Geol. 284, 351–362.
Kounoudis, R., Bastow, I.D., Ogden, C.S., Goes, S., Jenkins, J., Grant, B., Braham, C., 2020. Seismic tomographic imaging of the Eastern Mediterranean mantle: Implications for terminal-stage subduction, the uplift of Anatolia, and the development of the north Anatolian fault. Geochem. Geophys. Geosyst. 21.
Kyser, T.K., Kerrich, R., 1991. Retrograde exchange of hydrogen between hydrous minerals and water at low temperatures. In: Tayor, H.P., O'Neill, J.R., Kaplan, I.R. (Eds.), Stable Isotope Geochemistry: a Tribute to Samuel Epstein. The Geochemical Society Special Publication, San Antonio, pp. 409–422.
Kyser, T.K., O'Hanley, D.S., Wicks, F.J., 1999. The origin of fluids associated with serpentinization; evidence from stable-isotope compositions. Can. Mineral. 37, 223–237.
Mackenzie, G.D., Maguire, P.K.H., Coogan, L.A., Khan, M.A., Eaton, M., Petrides, G., 2006. Geophysical constraints on the crustal architecture of the Troodos ophiolite: results from the IANGASS project. Geophys. J. Int. 167, 1385–1401.
MacLeod, C.J., 1988. The Tectonic Evolution of the Eastern Limassol Forest Complex. PhD, Open University, Cyprus.
MacLeod, C.J., Allerton, S., Gass, I.G., Xenophontos, C., 1990. Structure of a fossil ridge–transform intersection in the Troodos ophiolite. Nature 348, 717–720.
MacLeod, C.J., Murton, B.J., 1993. Structure and tectonic evolution of the Southern Troodos Transform Fault Zone, Cyprus. Geol. Soc. Lond. Spec. Publ. 76, 141–176.
Magaritz, M., Taylor, H.P., 1974. Oxygen and hydrogen isotope studies of serpentinization in the Troodos ophiolite complex. Cyprus. Earth Planet. Sci. Lett. 23, 8–14.
Manzi, V., Lugli, S., Roveri, M., Dela, P.F., Gennari, R., Lozar, F., Natalicchio, M., Schreiber, B.C., Taviani, M., Turco, E., 2016. The Messinian salinity crisis in Cyprus: a further step towards a new stratigraphic framework for Eastern Mediterranean. Basin Res. 28, 207–236.
Martin, A.J., MacLeod, C.J., McFall, K.A., McDonald, I., Jamieson, J.W., Cox, S., 2023. Ultramafic-Hosted Ni-Cu-Co-(As) Mineralization from an Ancient Oceanic Transform Fault Zone in the Troodos Ophiolite, Cyprus: An Analogue for Ultramafic Sea-Floor Massive Sulfide Mineralization? Econ. Geol. 118, 1125–1147.
McArthur J. M., Howarth R. J. and Shield G. A. (2012) Strontium isotope stratigraphy. In The Geological Time Scale 2012 (ed. Gradstein F.M., Ogg J.G., Schmotz M.D., Ogg G. M). Elsevier, Amsterdam. pp. 127–144.
McCaig, A.M., Delacour, A., Fallick, A.E., Castelain, T., Früh-Green, G.L., 2010. Detachment fault control on hydrothermal circulation systems: Interpreting the subsurface beneath the TAG hydrothermal field using the isotopic and geological evolution of oceanic core complexes in the Atlantic. In: Geophysical Monograph Series Geophysical Monograph. American Geophysical Union, Washington, D. C, pp. 207–239.
McCallum, J.E., 1989. Sedimentation and tectonics of the Plio-Pleistocene of Cyprus. University of Edinburgh, PhD.
Mével, C., 2003. Serpentinization of abyssal peridotites at mid-ocean ridges. C. r. Geosci. 335, 825–852.
Miller D. J. and Christensen N. I. (1997) Seismic velocities of lower crustal and upper mantle rocks from the slow-spreading Mid-Atlantic Ridge, south of the Kane Transform zone (MARK). In Proc. ODP, Sci. Results, 153 (ed. Karson, J.A., Cannat, M., Miller, D.J., and Elthon, D). Ocean Drilling Program, College Station, Texas. pp. 437–454.
Moore, D.E., Rymer, M.J., 2007. Talc-bearing serpentinite and the creeping section of the San Andreas fault. Nature 448, 795–797.
Moores, E.M., Robinson, P.T., Malpas, J., Xenophonotos, C., 1984. Model for the origin of the Troodos massif, Cyprus, and other mideast ophiolites. Geology 12, 500–503.
Moores, E.M., Vine, F.J., 1971. The Troodos Massif, Cyprus and other Ophiolites as Oceanic Crust: Evaluation and Implications. Philos. Trans. R. Soc. A Math. Phys. Eng. Sci. 268, 443–467.
Mottl, M.J., McCollom, T.M., Wheat, C.G., Fryer, P., 2023. Chemistry of springs across the Mariana forearc: Carbon flux from the subducting plate triggered by the lawsonite-to-epidote transition? Geochim. Cosmochim. Acta 340, 1–20.
Mottl, M.J., Wheat, C.G., Fryer, P., Gharib, J., Martin, J.B., 2004. Chemistry of springs across the Mariana forearc shows progressive devolatilization of the subducting plate. Geochim. Cosmochim. Acta 68, 4915–4933.
Mukasa, S.B., Ludden, J.N., 1987. Uranium-lead isotopic ages of plagiogranites from the Troodos ophiolite, Cyprus, and their tectonic significance. Geology 15, 825.
Müller, R.D., Sdrolias, M., Gaina, C., Roest, W.R., 2008. Age, spreading rates, and spreading asymmetry of the world's ocean crust. Geochem. Geophys. Geosyst. 9.
Murton, B.J., 1986. Anomalous oceanic lithosphere formed in a leaky transform fault: evidence from the Western Limassol Forest Complex. Cyprus. J. Geol. Soc. London 143, 845–854.
Nielsen, S.G., Klein, F., Marschall, H.R., Pogge von Strandmann, P.A., Auro, M., 2024. Magnesium isotope fractionation processes during seafloor serpentinization and implications for serpentinite subduction. Solid Earth 15, 1143–1154.
Nuriel, P., Katzir, Y., Abelson, M., Valley, J.W., Matthews, A., Spicuzza, M.J., Ayalon, A., 2009. Fault-related oceanic serpentinization in the Troodos ophiolite, Cyprus: Implications for a fossil oceanic core complex. Earth Planet. Sci. Lett. 282, 34–46.
O'Hanley, D.S., Offler, R., 1992. Characterization of multiple serpentinization, Woodsreef, New South Wales. Can. Mineral. 30, 1113–1126.
O'Hanley, D.S., Schandl, E.S., Wicks, F.J., 1992. The origin of rodingites from Cassiar, British Columbia, and their use to estimate T and P(H_2O) during serpentinization. Geochim. Cosmochim. Acta 56, 97–108.
Peacock, S.M., 1987. Serpentinization and infiltration metasomatism in the Trinity peridotite, Klamath province, northern California: implications for subduction zones. Contrib. Mineral. Petrol. 95, 55–70.
Pearce, J.A., Lippard, S.J., Roberts, S., 1984. Characteristics and tectonic significance of supra-subduction zone ophiolites. Geol. Soc. Spec. Publ. 16, 77–94.
Peters, D., Bretscher, A., John, T., Scambelluri, M., Pettke, T., 2017. Fluid-mobile elements in serpentinites: Constraints on serpentinisation environments and element cycling in subduction zones. Chem. Geol. 466, 654–666.
Poole, A.J., Robertson, A.H.F., 1991. Quaternary uplift and sea-level change at an active plate boundary. Cyprus. J. Geol. Soc. London 148, 909–921.
Poole A. and Robertson A. (1998) Pleistocene fanglomerate deposition related to uplift of the Troodos Ophiolite, Cyprus. In Proc. ODP, Sci. Results, 160 (ed. Robertson, A.H. F., Emeis, K.C., Richter, C., and Camerlenghi, A.). Ocean Drilling Program, College Station, Texas. pp. 545–566.
Ranero, C.R., Morgan, J.P., McIntosh, K., Reichert, C., 2003. Bending-related faulting and mantle serpentinization at the Middle America trench. Nature 425, 367–373.
Ranero, C.R., Sallarès, V., 2004. Geophysical evidence for hydration of the crust and mantle of the Nazca plate during bending at the north Chile trench. Geology 32, 549–552.
Rautenschlein, M., Jenner, G.A., Hertogen, J., Hofmann, A.W., Kerrich, R., Schmincke, H. U., White, W.M., 1985. Isotopic and trace element composition of volcanic glasses from the Akaki Canyon, Cyprus: implications for the origin of the Troodos ophiolite. Earth Planet. Sci. Lett. 75, 369–383.
Robertson A. H. F. (1998a) Formation and destruction of the Eratosthenes Seamount, Eastern Mediterranean Sea, and implications for collisional processes. In Proc. ODP, Sci. Results, 160 (ed. Robertson, A.H.F., Emeis, K.C., Richter, C., and Camerlenghi, A.). Ocean Drilling Program, College Station, Texas. pp. 681–699.
Robertson A. H. F. (1998b) Mesozoic-Tertiary tectonic evolution of the easternmost Mediterranean area: integration of marine and land evidence. In Proc. Ocean Drill. Prog. Sci. Results, 160 (ed. Robertson, A.H.F., Emeis, K.C., Richter, C., and Camerlenghi, A.). Ocean Drilling Program, College Station, Texas. pp. 723–782.
Robertson, A.H.F., 1998. Tectonic significance of the Eratosthenes Seamount: a continental fragment in the process of collision with a subduction zone in the eastern Mediterranean (Ocean Drilling Program Leg 160). Tectonophysics 298, 63–82.
Robertson, A.H.F., 1977. Tertiary uplift history of the Troodos massif, Cyprus. GSA Bull. 88, 1763–1772.
Rouchy, J.M., Orszag-Sperber, F., Blanc-Valleron, M.-M., Pierre, C., Rivière, M., Combourieu-Nebout, N., Panayides, I., 2001. Paleoenvironmental changes at the Messinian–Pliocene boundary in the eastern Mediterranean (southern Cyprus basins): significance of the Messinian Lago-Mare. Sediment. Geol. 145, 93–117.
Schildgen, T.F., Cosentino, D., Frijia, G., Castorina, F., Dudas, F.Ö., Iadanza, A., Sampalmieri, G., Cipollari, P., Caruso, A., Bowring, S.A., Strecker, M.R., 2014. Sea level and climate forcing of the Sr isotope composition of late Miocene Mediterranean marine basins. Geochem. Geophys. Geosyst. 15, 2964–2983.
Schwarzenbach E. M., Früh-Green G. L., Bernasconi S. M., Alt J. C., Shanks W. C. III, Gaggero L. and Crispini L. (2012) Sulfur geochemistry of peridotite-hosted hydrothermal systems: Comparing the Ligurian ophiolites with oceanic serpentinites. Geochim. Cosmochim. Acta **91**, 283–305.
Scicchitano, M.R., Spicuzza, M.J., Ellison, E.T., Tuschel, D., Templeton, A.S., Valley, J. W., 2021. In situ oxygen isotope determination in serpentine minerals by SIMS: Addressing matrix effects and providing new insights on serpentinisation at hole BA1B (samail ophiolite, Oman). Geostand. Geoanal. Res. 45, 161–187.
Shelton, A.W., 1993. Troodos revisited: the Mount Olympus gravity anomaly. Geol. Soc. Spec. Publ. 76, 197–212.
Sheppard, S.M.F., 1980. Isotopic evidence for the origins of water during metamorphic processes in oceanic crust and ophiolite complexes. Coll. Int. C.N.R.S 135–147.
Snow, J.E., Hart, S.R., Dick, H.J., 1993. Orphan strontium-87 in abyssal peridotites: daddy was a granite. Science 262, 1861–1863.
Stow, D.A.V., Braakenburg, N.E., Xenophontos, C., 1995. The Pissouri Basin fan-delta complex, southwestern Cyprus. Sediment. Geol. 98, 245–262.
Teagle, D.A.H., Ildefonse, B., 2011. Journey to the mantle of the Earth. Nature 471, 437–439.
Templeton, A.S., Ellison, E.T., 2020. Formation and loss of metastable brucite: does Fe (II)-bearing brucite support microbial activity in serpentinizing ecosystems? Philos. Trans. A Math. Phys. Eng. Sci. 378, 20180423.
Ulrich, M., Muñoz, M., Boulvais, P., Cathelineau, M., Cluzel, D., Guillot, S., Picard, C., 2020. Serpentinization of New Caledonia peridotites: from depth to (sub-)surface. Contrib. Mineral. Petrol. 175, 91.
Vesin, C., Rubatto, D., Pettke, T., Deloule, E., 2023. Multistage hydration during oceanic serpentinisation revealed by in situ oxygen isotope and trace element analyses. Geochim. Cosmochim. Acta 355, 13–31.
Wenner, D.B., Taylor, H.P., 1974. D/H and O^{18}/O^{16} studies of serpentinization of ultramaflc rocks. Geochim. Cosmochim. Acta 38, 1255–1286.
Wenner, D.B., Taylor, H.P., 1973. Oxygen and hydrogen isotope studies of the serpentinization of ultramafic rocks in oceanic environments and continental ophiolite complexes. Am. J. Sci. 273, 207–239.
Wenner, D.B., Taylor, H.P., 1971. Temperatures of serpentinization of ultramafic rocks based on O^{18}/O^{16} fractionation between coexisting serpentine and magnetite. Contrib. Mineral. Petrol. 32, 165–185.
Wilson R. A. M. (1959) The geology of the Xeros-Troodos area. Authority of the Government of Cyprus.
Yamada, C., Tsujimori, T., Chang, Q., Kimura, J.I., 2019. Boron isotope variations of Franciscan serpentinites, northern California. Lithos 334–335, 180–189.